Accepted Manuscript

A variational constitutive model for slip-twinning interactions in hcp metals: application to single- and polycrystalline magnesium

Yingrui Chang, Dennis M. Kochmann

Please cite this article as: Chang, Y., Kochmann, D.M., A variational constitutive model for slip-twinning interactions in hcp metals: application to single- and polycrystalline magnesium, International Journal of Plasticity (2015), doi: 10.1016/j.ijplas.2015.03.008.

A variational constitutive model for slip-twinning interactions in hcp metals: application to single- and polycrystalline magnesium

Yingrui Chang, Dennis M. Kochmann*

Graduate Aerospace Laboratories, California Institute of Technology, Pasadena, CA 91125, U.S.A.

Abstract

We present a constitutive model for hcp metals which is based on variational constitutive updates of plastic slips and twin volume fractions and accounts for the related lattice reorientation mechanisms. The model is applied to single- and polycrystalline pure magnesium. We outline the finite-deformation plasticity model combining basal, pyramidal, and prismatic dislocation activity as well as a convexification-based approach for deformation twinning. A comparison with experimental data from single-crystal tension-compression experiments validates the model and serves for parameter identification. The extension to polycrystals via both Taylor-type modeling and finite element simulations shows a characteristic stress-strain response that agrees well with experimental observations for polycrystalline magnesium. The presented continuum model does not aim to represent the full details of individual twin-dislocation interactions; yet, it is sufficiently efficient to allow for finite element simulations while qualitatively capturing the underlying microstructural deformation mechanisms.

Keywords: plasticity, twinning, magnesium, polycrystal

1. Introduction

Magnesium and magnesium-based alloys have gained great technological importance due to their excellent strength-to-weight ratios, making them ideal candidates e.g. for the transportation industry or for defense applications. However, its hexagonal crystal structure furnishes Mg and its alloys with a non-trivial mechanical performance which involves a substantial tension-compression asymmetry (Ball and Prangnell, 1994; Avedesian and Baker, 1999; Lou et al., 2007; Kurukuri et al., 2014) and a comparably low ductility at low holonomous temperature (Hauser et al., 1956; Tegart, 1964), as well as a pronounced deformation anisotropy, see e.g. the recent studies of Agnew and Duygulu (2005); Lou et al. (2007); Stanford et al. (2011). Therefore, the successful implementation of Mg-based materials in everyday applications essentially hinges upon suitable models to accurately describe, to thoroughly understand, and to reliably predict the complex material response over wide ranges of loading and environmental conditions.

The origin of the complex mechanical response lies in the hcp crystallography of Mg with a specific lattice aspect ratio of $c/a = 1.624$ (Christian and Mahajan, 1995). While the crystal structure offers several slip systems that operate in the basal plane, it severely restricts out-of-plane dislocation activity due to relatively high critical resolved shear stresses of all non-basal systems, see e.g. (Staroselsky and Anand, 2003). Instead, if the sample is deformed parallel to the c-axis, stress relaxation can be accommodated by deformation twinning which, by itself, is fairly well understood and leads to a reorientation of the crystal lattice by rotations or reflections about characteristic twin systems (Christian and Mahajan, 1995). However, the coexistence of slip and twinning in Mg leads to a complex deformation behavior with rich microstructural phenomena that are responsible for the macroscopic response, cf. (Hauser et al., 1956; Reed-Hill and Robertson, 1958; Roberts and Partridge, 1966; Wonsiewicz and Backofen, 1967; Ando and Tonda, 2000). The exact deformation modes are still subject to controversial discussions which have raised a number of open questions, see e.g. (Lilleodden, 2010) for a more recent discussion.

---

*Corresponding author (phone +1-626-395-8113, fax +1-626-395-2900).
Email address:* `kochmann@caltech.edu` (Dennis M. Kochmann)

A variety of models operating on different length scales has been proposed to bridge the gap between macroscopic observations and microstructural mechanisms in Mg, from the atomistic level all the way up to continuum-mechanics descriptions. Here, we limit our scope to the latter and aim at incorporating as much lower-scale information about specific slip and twinning modes as necessary (but not more) to accurately and efficiently describe the effective response of single- and polycrystalline Mg. Since dislocation glide is one of the primary inelastic mechanisms, many models have borrowed concepts from conventional crystal plasticity (Hill, 1966; Rice, 1971; Asaro and Rice, 1977; Asaro, 1983; Simo, 1988a,b). Deformation twinning was included by introducing each twin system as an additional slip system (often referred to as *pseudo slip systems*) (Houtte, 1978; Kalidindi, 2001; Agnew et al., 2001; Staroselsky and Anand, 2003; Graff et al., 2007). Experiments on single- and polycrystalline Mg (Kelley and Hosford, 1968b,a) have confirmed the importance of the lattice reorientation due to twinning, which was not accounted for in those early models. In addition, the coexistence of untwinned and twinned domains and simultaneous activity of dislocations in both orientations can significantly affect the stress-strain response. Recently, several approaches have been reported that aim to overcome these deficiencies by including more microstructural details. Among those, closest to our model presented here are those of Homayonifar and Mosler (2011, 2012) and Zhang and Joshi (2012).

Homayonifar and Mosler (2011, 2012) presented variational models whose crystal plasticity basis is enriched by energy relaxation schemes to describe the effects of deformation twinning, cf. (James, 1981; Ball and James, 1987; Kochmann and Hackl, 2011). In this approach, the non-(quasi)convex energy landscape is replaced by either a rank-one-convex envelope (which is realized by sequential lamination to identify energy-minimizing fine-scale laminate patterns) (Ortiz and Repetto, 1999) or by full convexification (in which case lamellar patterns are free of the constraint of mechanical compatibility), see also (Glüge et al., 2010). While these approaches have a solid mathematical foundation and offer beneficial extensions and numerical advantages owing to the variational structure, they are also numerically costly and simulation examples have been limited to material point calculations due to the computational complexity. On the other hand, Zhang and Joshi (2012) introduced a crystal plasticity-based formulation with pseudo-slip systems to accommodate twinning, enriched by a lattice reorientation procedure to account for slip in both parent and twinned orientations. Their model accounts for many details of the slip-twinning interactions, yet it uses a conventional crystal plasticity formulation based on direct updates of the inelastic variables and therefore without a variational structure. Here, we combine both concepts into an efficient variational model for Mg accounting for slip-twinning interactions without the necessity of energy relaxation algorithms by using variational constitutive updates (Comi et al., 1991, 1992; Ortiz and Stainier, 1999).

Variational models offer various advantages from both a numerical-mathematical and a physical viewpoint. By using variational constitutive updates, the internal state variables and the deformation mapping follow from minimization of the same potential, which circumvents the complexity of having to solve for both types of variables simultaneously. In addition, the implicit update of the internal variables in the variational approach improves the efficiency by allowing for considerably larger time steps compared to explicit schemes, which in turn enables the simulation of significantly more complex physical scenarios. Owing to their underlying minimum principle, variational models also offer a convenient foundation for error estimation and mesh adaptation, see e.g. (Radovitzky and Ortiz, 1999; Thoutireddy and Ortiz, 2004; Mosler and Ortiz, 2006). The existence of solutions and the formation of fine-scale microstructure can be analyzed by well-established techniques, see e.g. (Ball and James, 1987; Ortiz and Repetto, 1999; Carstensen et al., 2002). Variational constitutive updates have been applied to a wide range of material models, including viscoelasticity and viscoplasticity (Ortiz and Stainier, 1999), crystal plasticity (Ortiz and Repetto, 1999; Ortiz et al., 2000; Carstensen et al., 2002), and strain gradient plasticity (Qiao, 2009); they also admit a variational, thermodynamically-consistent extension to thermo-mechanical coupling, see e.g. (Yang et al., 2006).

Our approach is similar in spirit and is based on variational constitutive updates to describe the slip-twinning interactions in Mg and Mg alloys (although we focus on pure Mg here, the presented framework can easily be extended to other hcp metals). Our model uses a finite-strain crystal plasticity formulation which accounts for the lattice reorientation due to twinning on the flow rule level similarly to (Zhang and Joshi, 2012). All prevailing slip and twin systems and interactions between them are accounted for by appropriate hardening energies and dissipation potentials. We validate our model and identify the required material parameters by direct comparison with the seminal experiments of Kelley and Hosford (1968b) on single-crystalline Mg. We then proceed to apply the model to polycrystalline Mg and predict the texture evolution during channel-die compression (comparable to experimental data of Kelley and Hosford (1968a)) and during cold rolling. Results include both material-point calculations as well as finite element studies to capture the effective response of representative polycrystalline samples.

2

2. Crystal plasticity framework for the interaction of slip and twinning

We begin by outlining the theoretical framework used in subsequent sections to describe the interactions of dislocation slip and deformation twinning in Mg on the single-crystal level. Here, rather than resolving individual twins and dislocations, we resort to plastic slips and twin volume fractions as the primary internal variables to describe the material's microstructure as done e.g. in (Agnew et al., 2001; Staroselsky and Anand, 2003; Graff et al., 2007; Zhang and Joshi, 2012; Homayonifar and Mosler, 2011, 2012). Therefore, we employ a crystal plasticity-based formulation in finite strains, cf. (Rice, 1971; Asaro and Rice, 1977; Asaro, 1983). We note that the general framework is sufficiently general to apply to any crystalline solid in which slip and twinning are the dominant plastic deformation mechanism. Let us first review the kinematic relations before presenting the variational approach based on concepts of Ortiz and Stainier (1999); Ortiz et al. (2000).

2.1. Kinematic description of the slip–twinning competition

Suppose the material's crystallography exhibits n_s slip systems denoted by (s_α, m_α) where s_α and m_α are unit vectors pointing into the direction of slip and being normal to the slip plane, respectively. Analogously, there exist n_t twin systems (a_β, n_β) with twin plane normal n_β and twinning shear direction a_β, see e.g. (Christian and Mahajan, 1995) for a review. Here and in the following, we use subscripts α and β to differentiate between slip and twin systems, respectively. As in conventional crystal plasticity models, dislocation activity is described by plastic slips $\gamma = \{\gamma_1, \ldots, \gamma_{n_s}\}$ acting across all n_s slip system. In addition, the effect of twinning is captured by the twinning ratios $\lambda = \{\lambda_1, \ldots, \lambda_{n_t}\}$ which describe the volume fractions of the twinned orientations. Obviously, the twin volume fractions are constrained by

$$0 \leq \lambda_\beta \leq 1 \quad \text{for} \quad \beta = 1, \ldots, n_t, \qquad \text{and} \qquad 0 \leq \sum_{\beta=1}^{n_t} \lambda_\beta \leq 1. \tag{1}$$

Thus, the primary internal variables are the slip amounts γ and twinning ratios λ. It is important to note that models based on this kinematic description do not qualify to describe the intricate details of individual twins that may arise on much smaller length scales than those of dislocations on the mesoscale of a polycrystal, cf. (Yu et al., 2012). Unlike e.g. phase field models for deformation twinning (Clayton and Knap, 2011, 2013) or explicit continuum models resolving individual twins (Kochmann and Le, 2009), the introduction of twin volume fractions allows us to decouple the length scales and to model the effective material response on the mesoscopic level. We note that the description of the inelastic phenomena in terms of plastic slips and twin volume fractions is only one possible strategy to represent the microstructural configuration and thus to model plastic deformation; see e.g. the related approaches based on dislocation densities (Arsenlis and Parks, 2002; Ma and Roters, 2004; Lee et al., 2010; Hansen et al., 2013; Bertin et al., 2013).

In finite strains, we may assume a multiplicative decomposition of the deformation gradient tensor $F = \text{Grad}\,\varphi$ (where $\varphi(X)$ denotes the deformation mapping) into elastic and inelastic parts, i.e.

$$F = F_e\,F_{in}, \tag{2}$$

where F_e and F_{in} denote the elastic and inelastic deformation gradients, respectively. Both slip and twinning contribute to the plastic deformation and the specific order of these two mechanisms is not obvious. Therefore, we adopt the approach of Kalidindi (2001) and work with a single inelastic deformation gradient F_{in} to incorporate both relaxation schemes rather than further splitting F_{in} multiplicatively into plastic slip and twinning components (Homayonifar and Mosler, 2011, 2012). This further implies that no kinematic interactions between slip an twinning are built into this decomposition but will be accounted for by the specific constitutive model presented below.

From (2) the velocity gradient tensor as well as its elastic and inelastic contributions follow as, respectively,

$$l = \dot{F}F^{-1} = l_e + l_{in} = l_e + F_e\,\tilde{l}_{in}\,F_e^{-1} \qquad \text{with} \qquad l_e = \dot{F}_e F_e^{-1}, \quad \tilde{l}_{in} = \dot{F}_{in} F_{in}^{-1}. \tag{3}$$

Since at mesoscopic time scales slip and twinning are assumed to occur simultaneously, we further split the inelastic velocity gradient into its slip and twinning contributions according to

$$\tilde{l}_{in} = \tilde{l}_p + \tilde{l}_{tw}, \tag{4}$$

3

The kinematic interactions of slip and twinning are built into the flow rule as follows. Upon deformation twinning, all slip systems (s_α, m_α) in the parent orientation are reflected across the twin interfaces onto the respective twin orientation. Hence, the re-oriented slip system $(s'_{\alpha\beta}, m'_{\alpha\beta})$, i.e. the original slip system (s_α, m_α) now re-oriented in twin orientation β, is given by

$$s'_{\alpha\beta} = Q_\beta s_\alpha, \quad m'_{\alpha\beta} = Q_\beta m_\alpha, \qquad \text{with} \quad Q_\beta = I - 2\, n_\beta \otimes n_\beta \tag{5}$$

(and no summation over repeated indices is implied here). Consequently, the flow rule for slip is modified from conventional crystal plasticity to account for dislocation activity on both the original slip systems and their twin-orientation counterparts. Extending concepts of Kalidindi (2001) and Zhang and Joshi (2012), we thus use the following flow rules for slip and twinning:

$$\tilde{l}_p = \sum_{\alpha=1}^{n_s} \dot{\gamma}_\alpha \left[\phi \left(1 - \sum_{\beta=1}^{n_t} \lambda_\beta \right) s_\alpha \otimes m_\alpha + \sum_{\beta=1}^{n_t} \phi(\lambda_\beta)\, s'_{\alpha\beta} \otimes m'_{\alpha\beta} \right], \tag{6a}$$

$$\tilde{l}_{tw} = \sum_{\beta=1}^{n_t} \dot{\lambda}_\beta\, \gamma_\beta^{tw}\, a_\beta \otimes n_\beta. \tag{6b}$$

Here, γ_β^{tw} is the twinning shear strain associated with system β, which we assume to be constant and which is determined from the material's crystallography. $\phi(\lambda)$ is a monotonically-increasing function that governs the switching between parent and twin orientations. For compatibility it must satisfy $\phi(0) = 0$ and $\phi(1) = 1$. Our numerical experiments have shown that the specific choice of $\phi(\lambda)$ has little impact on the microstructural evolution due to the specific mechanisms leading to slip and twinning. If a grain is oriented favorable for twinning, it will in most cases completely reorient from the untwinned into the twinned state before alternative relaxation mechanisms (usually basal plane slip systems) are activated. However, the specific choice of $\phi(\lambda)$ is only relevant as long as the twin volume fractions are evolving (in the purely untwinned or fully twinned states it is irrelevant). From our experience, there is no reason to define more complicated representations of $\phi(\lambda)$ than the simplest valid choice, which will be used in the following, viz. $\phi(\lambda) = \lambda$, and which reduces to the formulation of Zhang and Joshi (2012).

In order to capture plastic hardening due to slip, we introduce the accumulated plastic strains $\epsilon = (\epsilon_1, \ldots, \epsilon_{n_s})$, which are updated when slip occurs on any of the n_s slip systems (in parent and twin orientations) via

$$\dot{\epsilon}_\alpha = |\dot{\gamma}_\alpha| \quad \text{for } \alpha = 1, \ldots, n_s. \tag{7}$$

Altogether, these model assumptions imply that we account for slip in both untwinned and twinned orientations, and that dislocations are fully transferred between these two orientations. Also, both untwinned and twinned orientations contribute to plastic hardening. This is different than e.g. the recent model of Homayonifar and Mosler (2012) who assumed all dislocations are consumed by the moving twinning front and no dislocations are transferred from the untwinned to the twinned orientation.

2.2. Constitutive relations and variational framework

Like in conventional crystal plasticity the Helmholtz free energy density is assumed to decompose additively as

$$\begin{aligned} W(F, F_{in}, \epsilon, \lambda) &= W_e(F_e) + W_p(\epsilon) + W_{tw}(\lambda) \\ &= W_e(F_e) + W_{p,self}(\epsilon) + W_{p,lat}(\epsilon) + W_{tw,self}(\lambda) + W_{tw,lat}(\lambda), \end{aligned} \tag{8}$$

where W_e is the elastic strain energy density depending on $F_e = F F_{in}^{-1}$. W_p denotes the stored plastic energy density due to slip, which further decomposes into self-hardening and latent hardening contributions, $W_{p,self}$ and $W_{p,lat}$, respectively. Analogously, W_{tw} denotes the stored plastic energy density due to twinning, which contains self-hardening and latent hardening contributions, $W_{tw,self}$ and $W_{tw,lat}$, respectively. Specific choices of all energy densities for magnesium will be discussed in Section 3.

We cast the material model into a variational framework (Ortiz and Stainier, 1999), so that the evolution of the internal variables is governed by the principle of minimum dissipation potential, see e.g. (Carstensen et al., 2002;

4

Conti and Ortiz, 2008) for discussions and (Hackl and Fischer, 2008) for its relation to the principal of maximum dissipation. We introduce the dual (dissipation) potential $\Psi^*(\dot{\boldsymbol{\gamma}}, \dot{\boldsymbol{\lambda}})$ so that the internal variables follow from the principle of minimum dissipation potential (i.e. they minimize the total stress power):

$$0 \in \frac{\partial}{\partial \dot{\gamma}_\alpha}(\dot{W} + \Psi^*), \qquad 0 \in \frac{\partial}{\partial \dot{\lambda}_\beta}(\dot{W} + \Psi^*). \tag{9}$$

The differential inclusions are necessary when rate-independence is considered; in case of rate-dependent evolution laws, the differential inclusions may be replaced by equalities, see e.g. (Carstensen et al., 2002; Kochmann and Hackl, 2011). The dual potential is assumed to have contributions from slip and twinning in an additive fashion, generally

$$\Psi^*_{\mathrm{p}}(\dot{\boldsymbol{\epsilon}}) = \sum_{\alpha=1}^{n_s} \Psi^*_{\mathrm{p},\alpha}(\dot{\epsilon}_\alpha), \qquad \Psi^*_{\mathrm{tw}}(\dot{\boldsymbol{\lambda}}) = \sum_{\beta=1}^{n_t} \Psi^*_{\mathrm{tw},\beta}(\dot{\lambda}_\beta). \tag{10}$$

To arrive at the resulting evolution laws, let us expand the stress power as

$$\dot{W} + \Psi^* = \frac{\partial W_{\mathrm{e}}}{\partial \boldsymbol{F}_{\mathrm{e}}} \cdot \dot{\boldsymbol{F}}_{\mathrm{e}} + \frac{\partial W_{\mathrm{p}}}{\partial \boldsymbol{\epsilon}} \cdot \dot{\boldsymbol{\epsilon}} + \frac{\partial W_{\mathrm{tw}}}{\partial \boldsymbol{\lambda}} \cdot \dot{\boldsymbol{\lambda}} + \Psi^*_{\mathrm{p}}(\dot{\boldsymbol{\epsilon}}) + \Psi^*_{\mathrm{tw}}(\dot{\boldsymbol{\lambda}}). \tag{11}$$

From (3) and (6) it follows that

$$\dot{\boldsymbol{F}}_{\mathrm{e}} = \dot{\boldsymbol{F}}\boldsymbol{F}_{\mathrm{in}}^{-1} - \boldsymbol{F}_{\mathrm{e}}\dot{\boldsymbol{F}}_{\mathrm{in}}\boldsymbol{F}_{\mathrm{in}}^{-1} = \dot{\boldsymbol{F}}\boldsymbol{F}_{\mathrm{in}}^{-1} - \boldsymbol{F}_{\mathrm{e}}\left(\sum_\alpha \dot{\gamma}_\alpha \boldsymbol{p}_\alpha + \sum_\beta \dot{\lambda}_\beta \gamma_\beta^{\mathrm{tw}} \boldsymbol{a}_\beta \otimes \boldsymbol{n}_\beta \right), \tag{12}$$

where $\boldsymbol{p}_\alpha$ is an abbreviation for the average slip direction tensor for each slip system over all twinned orientations:

$$\boldsymbol{p}_\alpha = \phi\left(1 - \sum_\beta \lambda_\beta \right) \boldsymbol{s}_\alpha \otimes \boldsymbol{m}_\alpha + \sum_\beta \phi(\lambda_\beta) \, \boldsymbol{s}'_{\alpha\beta} \otimes \boldsymbol{m}'_{\alpha\beta}. \tag{13}$$

Furthermore, note that

$$\frac{\partial W_{\mathrm{e}}}{\partial \boldsymbol{F}_{\mathrm{e}}} = \frac{\partial W_{\mathrm{e}}}{\partial \boldsymbol{F}} \cdot \frac{\partial \boldsymbol{F}}{\partial \boldsymbol{F}_{\mathrm{e}}} = \boldsymbol{P}\boldsymbol{F}_{\mathrm{in}}^{\mathrm{T}}, \qquad \text{where} \qquad \boldsymbol{P} = \frac{\partial W}{\partial \boldsymbol{F}} = \frac{\partial W_{\mathrm{e}}}{\partial \boldsymbol{F}} \tag{14}$$

denotes the first Piola-Kirchhoff stress tensor. Overall, this leads to

$$\dot{W} + \Psi^* = \boldsymbol{P} \cdot \dot{\boldsymbol{F}} - \sum_{\alpha=1}^{n_s} \dot{\gamma}_\alpha \tau_\alpha^{\mathrm{p}} - \sum_{\beta=1}^{n_t} \dot{\lambda}_\beta \tau_\beta^{\mathrm{tw}} + \frac{\partial W_{\mathrm{p}}}{\partial \boldsymbol{\epsilon}} \cdot \dot{\boldsymbol{\epsilon}} + \frac{\partial W_{\mathrm{tw}}}{\partial \boldsymbol{\lambda}} \cdot \dot{\boldsymbol{\lambda}} + \Psi^*_{\mathrm{p}}(\dot{\boldsymbol{\epsilon}}) + \Psi^*_{\mathrm{tw}}(\dot{\boldsymbol{\lambda}}) \tag{15}$$

with the resolved shear stresses on the slip and twin systems, respectively,

$$\tau_\alpha^{\mathrm{p}} = \boldsymbol{\sigma}_M \cdot \boldsymbol{p}_\alpha \qquad \text{and} \qquad \tau_\beta^{\mathrm{tw}} = \gamma_\beta^{\mathrm{tw}} \boldsymbol{\sigma}_M \cdot (\boldsymbol{a}_\beta \otimes \boldsymbol{n}_\beta) \tag{16}$$

and the Mandel stress tensor

$$\boldsymbol{\sigma}_M = \boldsymbol{F}_{\mathrm{e}}^{\mathrm{T}} \boldsymbol{P} \boldsymbol{F}_{\mathrm{in}}^{\mathrm{T}}. \tag{17}$$

Finally, application of principle (9) yields the evolution laws for the internal variables:

$$0 \in -|\tau_\alpha^{\mathrm{p}}| + \frac{\partial W_{\mathrm{p}}}{\partial \epsilon_\alpha} + \frac{\partial \Psi^*_{\mathrm{p},\alpha}}{\partial \dot{\epsilon}_\alpha}, \tag{18a}$$

$$0 \in -\tau_\beta^{\mathrm{tw}} + \frac{\partial W_{\mathrm{tw}}}{\partial \lambda_\beta} + \frac{\partial \Psi^*_{\mathrm{tw},\beta}}{\partial \dot{\lambda}_\beta}. \tag{18b}$$

The missing norm in the evolution law for the twinning volume fractions is only valid as long as $\lambda_\beta = 0$, to implement the polarity of twinning. That is, in contrast to slip which may occur in either positive or negative direction, twinning is restricted to occur in only one direction per twin system for crystallographic reasons, see e.g. (Christian and Mahajan,

5

1995). This, of course, changes as soon as $\lambda_\beta > 0$, so that a reversal of the loading can lead to detwinning (which implies $\dot{\lambda}_\beta < 0$), see e.g. (Lou et al., 2007). Also, we have neglected the dependence of the average slip direction tensor $\boldsymbol{p}_\alpha$ on the rates of the twinning ratios $\dot{\lambda}_\beta$, which is a valid assumption when considering small incremental steps in our numerical setup.

Experiments have found evidence for higher-order twin patterns, i.e. the activity of a second twin system in already-twinned domains of the crystal, see e.g. Hong et al. (2010); Kadiri et al. (2013). However, how such competing twin systems develop (e.g. in which order they are activated and whether or not they evolve simultaneously) is not entirely clear. Our model assumes that at a given instance of time only one twin system is evolving at any material point. This does not rule out that the crystal twins on one system and, as soon as the reorientation is complete, another twin system can be activated to result in the coexistence of multiple twin variants in the final deformed state.

To model twinning within an already twinned domain on a second system, we need to consider the reorientation of already twinned crystal by the newly-activated twin system. Since there is no limitation to the number of activatable twin systems, this could lead to a highly recursive mechanism and the resulting cross-interactions between the twin and slip systems soon become numerically demanding, if not intractable, especially within an implicit, variational framework. Therefore, we neglect the possibility of multiple twin variants evolving at the same time at any given material point for the sake of a fully implicit, variational formulation that covers many other phenomena observed experimentally, as shown later. Of course, this is a simplification of physical reality. In Taylor-type polycrystal simulations, this implies that only one twin variant is evolving at a time within each grain. In contrast, for mesoscale finite-element simulations that resolve the grain structure geometrically, the assumption demands that only one twin system is active at a time at each material point, thus allowing for (spatially-separated) multiple twin variants within a grain. While the restriction to only one active system is not a stringent necessity of the variational approach, it greatly reduces the model complexity, thus allowing for more efficient simulations. Many of the previously proposed models, see e.g. (Homayonifar and Mosler, 2011, 2012; Zhang and Joshi, 2012), use similar flow rules and reorientation schemes as presented here.

3. Specific choices of energetics and kinematics for pure magnesium

3.1. Elastic energy: polyconvex strain energy density

Here and in the following, we use conventional Miller indices to describe planes and orientations in the hexagonal lattice structure whose coordinate system be defined by the three basal unit vectors $\{\boldsymbol{a}_1, \boldsymbol{a}_2, \boldsymbol{a}_3\}$ with $\boldsymbol{a}_3 = -(\boldsymbol{a}_1 + \boldsymbol{a}_2)$ and the longitudinal axis with unit vector $\boldsymbol{c} = \{0, 0, 0, 1\}$. Due to its hcp crystallography, the elastic response of Mg exhibits transverse isotropy (with isotropy in the basal plane). Almost all previous models for Mg used isotropic strain energy densities to approximate the elastic response, a common albeit simplifying approximation, see e.g. the discussion in (Clayton and Knap, 2011). Here, in addition to capturing the anisotropic elastic behavior of hcp metals, we aim to construct a polyconvex energy density for the following reasons. At finite strains, the loss of quasiconvexity of the free energy density can lead to the loss of stability of a homogeneous deformation gradient and to the formation of fine-scale microstructure (so-called minimizing sequences), see e.g. (Ball, 1976; Ball and James, 1987; Ortiz and Repetto, 1999; Mielke, 2004; Conti and Theil, 2005). Quasiconvexity is hard to enforce owing to its non-local definition. A reasonable alternative is the use of polyconvex energy densities since polyconvexity (of a finite-valued, continuous function) implies quasiconvexity which, in turn, ensures rank-one convexity thus avoiding instability due to loss of ellipticity under large deformation. Here, we adopt the polyconvex energy density proposed by Schröder et al. (2008) and adjust it to describe the transversely-isotropic response of magnesium.

We assume the additive decomposition of the strain energy density into isotropic and anisotropic parts and we adopt the material frame-indifferent form

$$W_{\mathrm{e}}(\boldsymbol{F}) = W_{\mathrm{iso}}(I_1, I_2, I_3) + W_{\mathrm{aniso}}(J_4, J_5) \tag{19}$$

6

	C_{11}	C_{33}	C_{44}	C_{13}	C_{12}	C_{66}
experimental:	59.74	62.00	16.59	21.48	25.65	17.05
model:	59.72	57.26	17.27	21.93	25.81	16.95

Table 1: Experimentally-determined transversely-isotropic elastic constants of pure Mg at 280 K (all values in GPa), from (Slutsky and Garland, 1957) as well as the corresponding elastic constants of the polyconvex energy density.

with invariants of the right Cauchy-Green tensor $C = F^{\mathrm{T}}F$ defined by

$$I_1 = \operatorname{tr} C,$$
$$I_2 = \operatorname{tr}(\operatorname{Cof} C),$$
$$I_3 = \det C,$$
$$J_4 = \operatorname{tr}(CG),$$
$$J_5 = \operatorname{tr}\left[(\operatorname{Cof} C)G\right]$$

and the cofactor operator defined via $\operatorname{Cof} A = (\det A)A^{-\mathrm{T}}$. Metric tensor G depends on the specific material symmetry, which in case of hcp materials is given by

$$G = \operatorname{diag}(1, 1, C^2) \qquad \Rightarrow \qquad \operatorname{Cof} G = \operatorname{diag}(C^2, C^2, C^4). \tag{20}$$

For magnesium we have $C = c/a = 1.624$ where a and c denote the length of the basal-plane's Burgers vector in the $\langle 11\bar{2}0 \rangle$ direction and the hcp unit cell height, respectively. Following Schröder et al. (2008), our specific choices of the isotropic and anisotropic energy densities are

$$W_{\mathrm{iso}}(I_1, I_2, I_3) = \alpha_1 I_1 + \alpha_2 I_2 + \delta_1 I_3 - \delta_2 \log \sqrt{I_3}, \tag{21}$$
$$W_{\mathrm{aniso}}(J_4, J_5) = \frac{\eta_1}{\alpha_4 \, g^{\alpha_4}}\left(J_4^{\alpha_4}, + J_5^{\alpha_4}\right), \tag{22}$$

for which the constraints of ellipticity and a stress-free reference configuration impose the restrictions

$$\alpha_1 > 0, \qquad \alpha_2 > 0, \qquad \delta_1 > 0, \qquad \eta_1 > 0, \qquad \alpha_4 > 1, \qquad \delta_2 = 2\alpha_1 + 4\alpha_2 + 2\delta_1 + 2\eta_1. \tag{23}$$

To fit these unknown elastic material parameters to experimental data, we compute the components of the elastic modulus tensor

$$\mathbb{C}_{IJKL}(F) = 8 \frac{\partial W_{\mathrm{e}}}{\partial C_{IJ} \partial C_{KL}}(F), \tag{24}$$

which yields the following elastic moduli in the undeformed ground state:

$$\mathbb{C}_{IJKL}(I) = 4(\alpha_2 + \delta_1 + \alpha_4\eta_1)\delta_{IJ}\delta_{KL} + 2(\alpha_1 + \alpha_2)(\delta_{IK}\delta_{JL} + \delta_{IL}\delta_{JK})$$
$$+ 2\frac{\eta_1}{g}\left[G_{JK}\delta_{LI} + G_{JL}\delta_{IK} + G_{IL}\delta_{JK} + G_{IK}\delta_{LJ} - 2\alpha_4(\delta_{IJ}G_{KL} + G_{IJ}\delta_{KL})\right] + 8(\alpha_4 - 1)\frac{\eta_1}{g^2}G_{IJ}G_{KL}$$

with $g = \operatorname{tr} G = 2 + C^2$. Notice that in the isotropic case ($G = I$), we recover the isotropic form with Lamé moduli

$$\lambda = 4(\alpha_2 + \delta_1 + \alpha_4\eta_1), \qquad \mu = 2(\alpha_1 + \alpha_2). \tag{25}$$

7

Using the specific form (20) for hcp crystals, the components of the elasticity tensor become (in Voigt notation)

$$C_{11} = \mathbb{C}_{1111} = 4\left[\alpha_1 + 2\alpha_2 + \delta_1 + \alpha_4\eta_1 - \frac{2a^2(a^2 + c^2)(\alpha_4 - 1)\eta_1}{(2a^2 + c^2)^2}\right], \tag{26}$$

$$C_{33} = \mathbb{C}_{3333} = 4\left[\alpha_1 + 2\alpha_2 + \delta_1 + \alpha_4\eta_1 - \frac{4a^2c^2(\alpha_4 - 1)\eta_1}{(2a^2 + c^2)^2}\right], \tag{27}$$

$$C_{44} = \mathbb{C}_{2323} = 2\left[\alpha_1 + \alpha_2 + \eta_1 - \frac{a^2\eta_1}{2a^2 + c^2}\right], \tag{28}$$

$$C_{13} = \mathbb{C}_{1133} = 4\left[\alpha_2 + \delta_1 + \frac{a^2\eta_1\left(2\alpha_4 a^2 + (3\alpha_4 - 2)c^2\right)}{(2a^2 + c^2)^2}\right], \tag{29}$$

$$C_{12} = \mathbb{C}_{1122} = 4\left[\alpha_2 + \delta_1 + \frac{\eta_1\left(2a^4(\alpha_4 - 1) + \alpha_4(2a^2 + c^2)c^2\right)}{(2a^2 + c^2)^2}\right], \tag{30}$$

$$C_{66} = \mathbb{C}_{1212} = 2\left[\alpha_1 + \alpha_2 + \frac{2a^2\eta_1}{2a^2 + c^2}\right]. \tag{31}$$

To confirm transverse isotropy, we note that the chosen form of the energy density satisfies automatically

$$C_{66} = \frac{C_{11} - C_{12}}{2}. \tag{32}$$

The elastic moduli have been fit to those determined experimentally by Slutsky and Garland (1957) shown in Table 1, which results in the material parameters for the polyconvex strain energy density summarized in Table 2. Table 1 also contains the experimental data for comparison. With the exception of C_{33}, the anisotropic elastic moduli are well captured by the chosen strain energy density, which is deemed sufficient for subsequent simulations.

α_1	α_2	δ_1	δ_2	α_4	η_1
4.82	3.46	0.06	23.76	10.0	0.45

Table 2: Best-fit results for the parameters used in the polyconvex strain energy density (all values in GPa except dimensionless α_4).

3.2. Inelastic deformation mechanism in pure magnesium

From all possible slip systems, basal slip is the dominant mode in Mg due to the significantly lower critical resolved shear stresses on basal slip systems with slip directions {11$\bar{2}$0} and slip plane normal {0001}. In addition, prismatic and pyramidal $\langle a \rangle$ slip systems are frequently observed when the activation of basal slip is suppressed (Burke and Hibbard, 1952; Reed-Hill and Robertson, 1958). Since the slip directions of these three systems all lie within the basal plane, they can operate on only four independent shear systems, which is insufficient to accommodate arbitrary plastic straining (von Mises, 1928; Taylor, 1938). Therefore, pyramidal $\langle c + a \rangle$ slip has been identified as a further slip mode active in Mg, see e.g. (Obara et al., 1973; Ando and Tonda, 2000), in particular to accommodate compression along the c-axis. The various types of slip systems are illustrated in Figure 1 and summarized in Table 3.

Some of the previous models for Mg have incorporated only a subset of the aforementioned slip systems due to redundancy and in order to reduce computational complexity and costs. In particular, the inclusion of pyramidal $\langle c + a \rangle$ slip was shown to beneficially reproduce experimental results, see e.g. (Agnew et al., 2001). On the other hand, prismatic and pyramidal $\langle a \rangle$ slips show quite similar effects to the prismatic ones (Agnew et al., 2006; Chapuis and Driver, 2011) but at considerably higher resolved shear stresses. Therefore, we choose to not include the pyramidal $\langle a \rangle$ systems. Overall, our set of modeled slip systems is thus given by the basal, prismatic and pyramidal $\langle c + a \rangle$ systems, which already provided realistic results for alloy AZ31B (Agnew et al., 2003; Agnew and Duygulu, 2005).

Deformation twinning is the most common mechanism in Mg to allow plastic deformation along the c-axis (requiring considerably lower activation stresses than the aforementioned non-basal slip systems). The most frequently
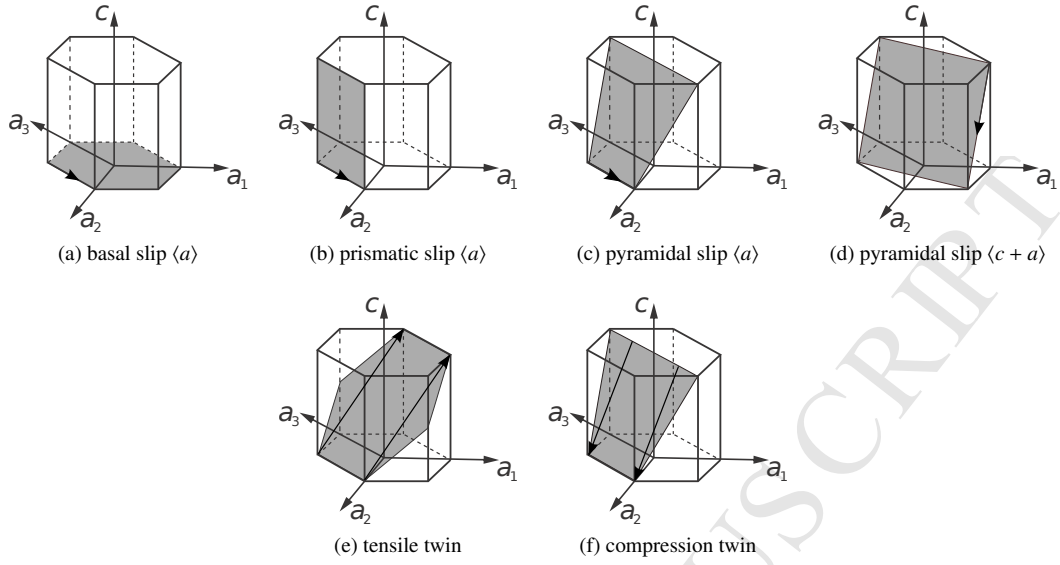
Figure 1: Schematic view of the primary slip and twin systems observed in Mg.

observed twinning mode in Mg is the $\{10\bar{2}1\}\langle\bar{1}011\rangle$ tensile twin system, which is activated when the c-axis is in tension. The critical shear strain associated with this twinning mode for pure Mg is $\gamma_{\text{tw}} = 0.1295$ (Christian and Mahajan, 1995). Furthermore, compression twinning can be observed when the c-axis is in compression (Kelley and Hosford, 1968b; Barnett, 2007). However, as pointed out e.g. by Zhang and Joshi (2012) and as seen in experiments (Brown et al., 2005), this twinning mode is difficult to activate due to its much higher critical resolved shear stress and large critical shear strain. Tensile twins are considerably easier to nucleate and their mobility is significantly higher, too, which can be explained by the differences in the twinning dislocation core structures of tensile and compressive twinning (Christian and Mahajan, 1995). The relevant twin systems to be included in our model are included in Table 3 along with their critical shear strains. As an important difference between slip and twinning, dislocations are free to glide in either positive or negative direction, whereas twinning is only allowed to occur in the twinning direction. This fact is automatically accounted for in the model presented here due to the twinning description via volume fractions. We will discuss the relevance of the tension and compression twin systems later in our numerical examples.

3.3. Stored energy: choice of hardening energies and dissipation potentials

The mechanical resistance differs dramatically between the various slip and twin systems, which leads to the observed highly-anisotropic plastic response. These differences are captured in the model by the hardening energies and associated dissipation potentials for all slip and twin system. Plastic work is stored in self-energy of each slip

type	slip/twin plane	slip/twinning direction	number of systems	γ_{tw}
basal slip:	$\{0001\}$	$\langle 11\bar{2}0\rangle$	3	-
prismatic slip:	$\{1\bar{1}00\}$	$\langle 11\bar{2}0\rangle$	3	-
pyramidal slip $\langle a\rangle$:	$\{1\bar{1}01\}$	$\langle 11\bar{2}0\rangle$	6	-
pyramidal slip $\langle c + a\rangle$:	$\{11\bar{2}2\}$	$\langle\bar{1}\bar{1}23\rangle$	6	-
tensile twin:	$\{10\bar{1}2\}$	$\langle\bar{1}011\rangle$	6	0.129
compression twin (rare):	$\{10\bar{1}1\}$	$\langle\bar{1}012\rangle$	6	1.066

Table 3: Properties of the various slip and twin systems found in Mg and included in the model.

9

system and in interaction energy. For the self-energy, we assume the general representation

$$W_{p,self}(\boldsymbol{\epsilon}) = \sum_{\alpha} \sigma_{\alpha}^{\infty} \left[\epsilon_{\alpha} + \frac{\sigma_{\alpha}^{\infty}}{h_{\alpha}} \exp\left(-\frac{h_{\alpha}\,\epsilon_{\alpha}}{\sigma_{\alpha}^{\infty}} \right) \right], \tag{33}$$

whose parameters differ between systems. The exponential law mimics Voce hardening (Agnew et al., 2001; Graff et al., 2007) and is well suited to describe the high-resistance of non-basal slip systems in hcp metals (Homayonifar and Mosler, 2011). σ_{α}^{∞} is the ultimate stress on each system, and h_{α} captures the corresponding hardening rate. In practice, small σ_{α}^{∞} and large h_{α} will result in a low activation. The slip hardening response is completed by assuming linear latent hardening, which implies

$$W_{p,lat}(\boldsymbol{\epsilon}) = \frac{1}{2}\boldsymbol{\epsilon} \cdot \mathcal{H}\boldsymbol{\epsilon}, \tag{34}$$

where $\mathcal{H}$ is a symmetric matrix containing the hardening moduli on its off-diagonals (and having a zero diagonal).

The rate dependence of all slip systems is accounted for by a power-law dissipation potential commonly used in crystal plasticity, see e.g. (Ortiz and Stainier, 1999),

$$\Psi_p^*(\dot{\boldsymbol{\gamma}}) = \sum_{\alpha} \frac{\tau_0 \dot{\gamma}_0}{m+1} \left(\frac{\dot{\gamma}_{\alpha}}{\dot{\gamma}_0} \right)^{m+1}. \tag{35}$$

with material constants τ_0, $\dot{\gamma}_0$ and m (one set of these for each slip system).

The tensile twin system is activated when the c-axis is in tension. Zhang and Joshi (2012) assumed a hard threshold for its activation. Beyond this yield point, they assumed that the resolved shear stress stress remains constant, which essentially implies a linear growth of the stored energy without hardening. Here, we take a different standpoint and assume linear hardening and linear rate dependence, i.e. we choose quadratic forms for both the hardening energy. For comparison, the similar formulation of Homayonifar and Mosler (2011) used a linear twin hardening energy. The associated dissipation potential must describe the rate-dependence of twinning. The recent work of Ulacia et al. (2010) shows a very low sensitivity of twinning in Mg alloys, and even negative strain rate sensitivity has been reported (Chun and Davies, 2011); see also the discussion in (Li and Ma, 2009) about twinning in Mg as a dissipative vs. elastic reshuffling process. To account for the low rate sensitivity, we here set the dissipation potential associated with twinning to zero. In summary, this results in

$$W_{tw}(\boldsymbol{\lambda}) = \sum_{\beta} \frac{1}{2} h_{\beta} \lambda_{\beta}^2 + \frac{1}{2} \boldsymbol{\lambda} \cdot \mathcal{K}\boldsymbol{\lambda}, \tag{36a}$$

$$\Psi_{tw}^*(\dot{\boldsymbol{\lambda}}) = 0, \tag{36b}$$

where h_{β} is the hardening parameter of twin system β, and $\mathcal{K}$ denotes the matrix containing all cross-hardening moduli.

To illustrate the different hardening laws and associated stress-strain responses, we perform a simple-shear test with only a single active system by aligning the slip or twinning direction with the macroscopic shear direction. The resulting stress-strain curves are shown in Figure 2. Obviously, basal slip and tensile twinning are easiest to activate, whereas prismatic and pyramidal slip require higher stress levels. Note that (in the absence of slip) the twinning curve becomes elastic once the twin volume fraction has reached 1 and the crystal is fully twinned. The material parameters used for these simulations have been determined by fitting experiments, which will be discussed in Section 4.1.

4. Numerical realization: variational constitutive updates

To make the theory amenable for numerical implementations, we introduce variational constitutive updates for discrete (constant) time steps Δt by defining an incremental energy density (Ortiz and Stainier, 1999; Ortiz et al., 2000)

$$\mathcal{F}(\boldsymbol{F}^{n+1}, \Delta\boldsymbol{\gamma}, \Delta\boldsymbol{\lambda}; \boldsymbol{F}_{in}^n, \boldsymbol{\epsilon}^n, \boldsymbol{\lambda}^n) = W(\boldsymbol{F}^{n+1}, \boldsymbol{F}_{in}^{n+1}, \boldsymbol{\epsilon}^n + |\Delta\boldsymbol{\gamma}|, \boldsymbol{\lambda}^n + \Delta\boldsymbol{\lambda}) - W(\boldsymbol{F}^n, \boldsymbol{F}_{in}^n, \boldsymbol{\epsilon}^n, \boldsymbol{\lambda}^n)$$
$$+ \Delta t\, \Psi_t^* \left(\frac{|\Delta\boldsymbol{\gamma}|}{\Delta t} \right) + \Delta t\, \Psi_{tw}^* \left(\frac{|\Delta\boldsymbol{\lambda}|}{\Delta t} \right), \tag{37}$$
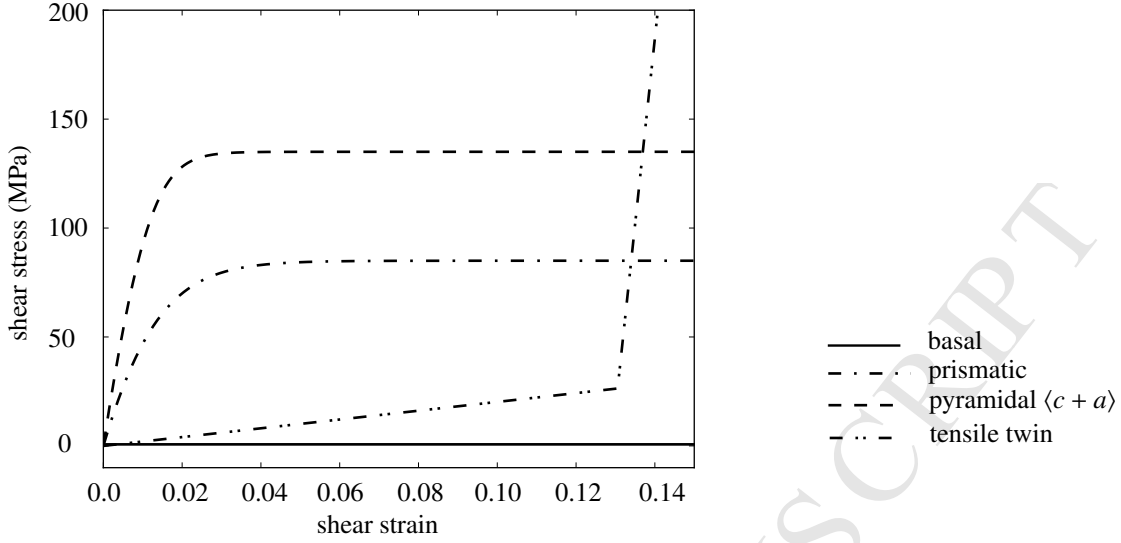
10

Figure 2: Hardening response of the different hardening energies

where superscript $(\cdot)^n$ denotes a quantity evaluated at time t^n, and $t^{n+1} = t^n + \Delta t$. The discretization of the flow rule follows a forward Euler scheme and approximates $\boldsymbol{F}_{\text{in}}^{n+1}$ by

$$\boldsymbol{F}_{\text{in}}^{n+1} = \text{dev}\left(\sum_\alpha \Delta\gamma_\alpha\, \boldsymbol{p}_\alpha^n + \sum_\beta \Delta\lambda_\beta\, \gamma_\beta^{\text{tw}}\, \boldsymbol{a}_\beta \otimes \boldsymbol{n}_\beta + \boldsymbol{I}\right) \boldsymbol{F}_{\text{in}}^n, \tag{38}$$

where we take the deviatoric part of the flow rule increment to insure isochoric inelastic deformation. Thus given $\boldsymbol{\epsilon}^n, \boldsymbol{\lambda}^n, \boldsymbol{F}_{\text{in}}^n$ at the old time t^n, and the new deformation gradient $\boldsymbol{F}^{n+1}$, the incremental updates of the internal variables at time t^{n+1} are obtained by minimization of (37), i.e.

$$(\Delta\boldsymbol{\gamma}, \Delta\boldsymbol{\lambda}) = \arg\min\, \mathcal{F}(\boldsymbol{F}^{n+1}, \Delta\boldsymbol{\gamma}, \Delta\boldsymbol{\lambda}; \boldsymbol{F}_{\text{in}}^n, \boldsymbol{\epsilon}^n, \boldsymbol{\lambda}^n), \tag{39}$$

which is the time-discrete version of the flow rules in (9). The internal variables at time t^{n+1} follow as

$$\boldsymbol{\gamma}^{n+1} = \boldsymbol{\gamma}^n + \Delta\boldsymbol{\gamma}, \qquad \boldsymbol{\epsilon}^{n+1} = \boldsymbol{\epsilon}^n + |\Delta\boldsymbol{\gamma}|, \qquad \boldsymbol{\lambda}^{n+1} = \boldsymbol{\lambda}^n + \Delta\boldsymbol{\lambda}. \tag{40}$$

This results in the condensed strain energy density

$$W_{\text{cond}}(\boldsymbol{F}^{n+1}; \boldsymbol{F}_{\text{in}}^n, \boldsymbol{\epsilon}^n, \boldsymbol{\lambda}^n) = \inf_{\Delta\boldsymbol{\gamma}, \Delta\boldsymbol{\lambda}}\left\{\mathcal{F}(\boldsymbol{F}^{n+1}, \Delta\boldsymbol{\gamma}, \Delta\boldsymbol{\lambda}; \boldsymbol{F}_{\text{in}}^n, \boldsymbol{\epsilon}^n, \boldsymbol{\lambda}^n)\, :\, 0 \le \lambda^n + \Delta\lambda \le 1\right\}, \tag{41}$$

and the corresponding first Piola-Kirchhoff stress tensor

$$\boldsymbol{P}^{n+1} = \frac{\partial W_{\text{cond}}}{\partial \boldsymbol{F}^{n+1}}(\boldsymbol{F}^{n+1}; \boldsymbol{F}_{\text{in}}^n, \boldsymbol{\epsilon}^n, \boldsymbol{\lambda}^n). \tag{42}$$

Therefore, this variational approach is not based on explicit updates of the internal variables but uses the above (implicit) variational framework.

The above scheme is implemented in a predictor-corrector fashion, and the minimization problem is solved by a projected line search algorithm, i.e., during iterations for a given time step we repeatedly project the updated internal variables onto the constraint set. The search direction is determined by a conventional Newton-Raphson scheme. As discussed before, for physical reasons we only admit the activation of one twin system at a time, which is realized numerically by projecting the non-zero twinning ratio to the interval $[0, 1]$. Material point calculations and finite element simulations were performed using an in-house code with variational structure.

11

hardening and dissipation parameters		
basal	h_α(MPa)	7100
	σ_∞(MPa)	0.7
	h_{ij}(MPa)	0.0
	τ_0(MPa)	1.75
	m	0.05
	$\dot{\gamma}_0$(s^{-1})	1.0
prismatic	h_α(MPa)	9000
	σ_∞(MPa)	85
	h_{ij}(MPa)	20
	τ_0(MPa)	1.75
	m	0.05
	$\dot{\gamma}_0$(s^{-1})	1.0
pyramidal	h_α(MPa)	30000
	σ_∞(MPa)	150
	h_{ij}(MPa)	25.0
	τ_0(MPa)	1.75
	m	0.05
	$\dot{\gamma}_0$(s^{-1})	1.0
tensile twin	h_0(MPa)	1.7
	k_{ij}(MPa)	40000

Table 4: Material parameters of the hardening energies and dissipation potentials for the slip and twin systems.

4.1. Parameter identification and model validation

The numerical model summarized in previous sections contains a large number of material parameters that require identification; in particular the 12 slip and 6 twin systems require individual parameters to be determined before running complex polycrystalline simulations. Kelley and Hosford (1968b) performed a series of elaborate plane-strain compression tests on pure single-crystalline Mg at room temperature, whose results will be used to determine the model parameters for each system. By carefully orienting the loading with respect to the hcp lattice, different slip and twin systems were activated in each case. Here, we numerically reproduce six loading scenarios from their experiments to calibrate the parameters of the independent slip and twin systems. All simulations are performed as material-point calculations under quasistatic conditions. The imposed deformation corresponds to a velocity gradient

$$\boldsymbol{l} = \begin{bmatrix} l_{11} & l_{12} & l_{13} \\ 0 & 0 & 0 \\ 0 & 0 & \dot{\varepsilon} \end{bmatrix}, \tag{43}$$

where the loading is in the 3-direction and characterized by loading rate $\dot{\varepsilon}$, while the sample is constrained in the transverse 2-direction. The unknown deformation in the 1-direction is found by solving for traction-free boundary conditions. These conditions are closest to experimental reality and do not impose the full deformation gradient as is frequently done in the literature for convenience.

The calibrated parameters for the 12 slip systems and 6 twin systems are summarized in Table 4. The corresponding numerical results are shown in Figures 3 and 4 along with experimental data from (Kelley and Hosford, 1968b) for comparison. The relative contributions of the various microstructural modes (defined as the ratio of each internal variable to the sum of the all internal variables) are also included to demonstrate the activated slip and twin systems. The labeling of the individual load cases corresponds to the original orientations reported by Kelley and Hosford (1968b).

- **Compression along the ⟨0001⟩-axis**:

    In loading cases a and b, the loading direction is along the ⟨0001⟩-axis. These two loading scenarios are theoretically prone to activate the compression twin system, which, however, is rarely observed experimentally
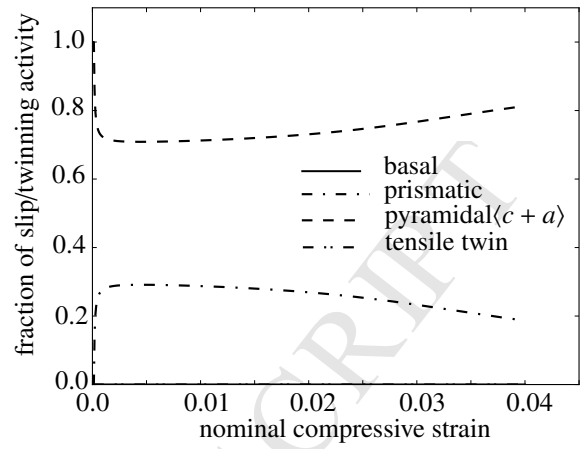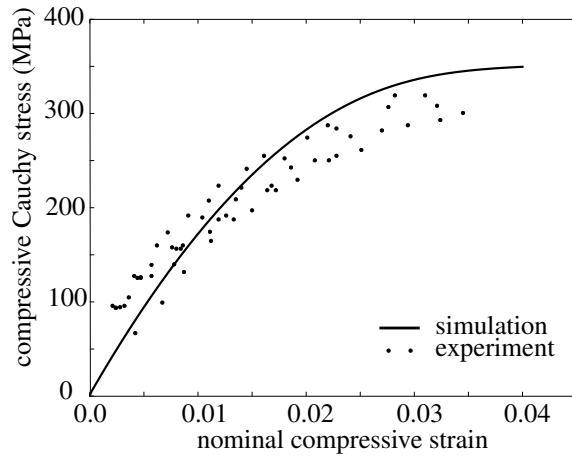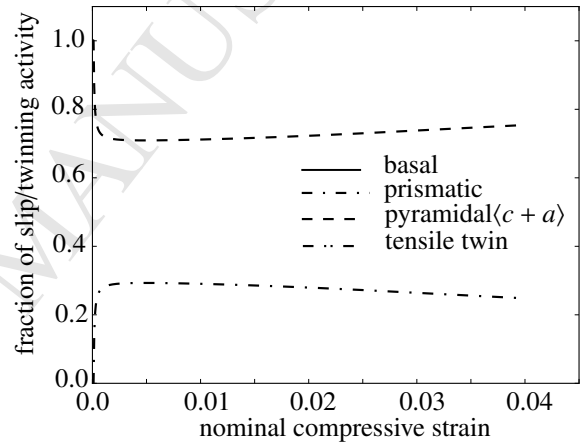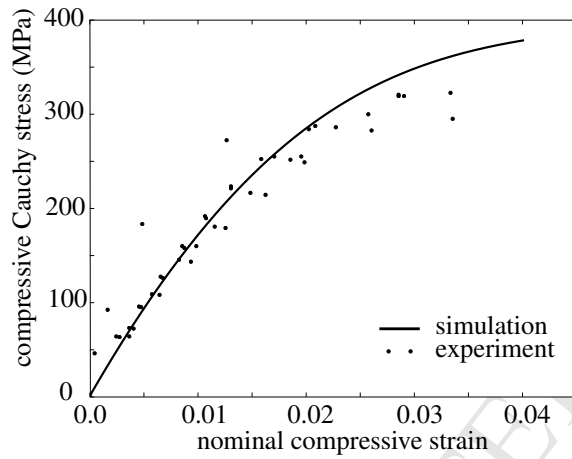
12

Case a: compression along the ⟨0001⟩-axis.

Case b: compression along the ⟨0001⟩-axis.
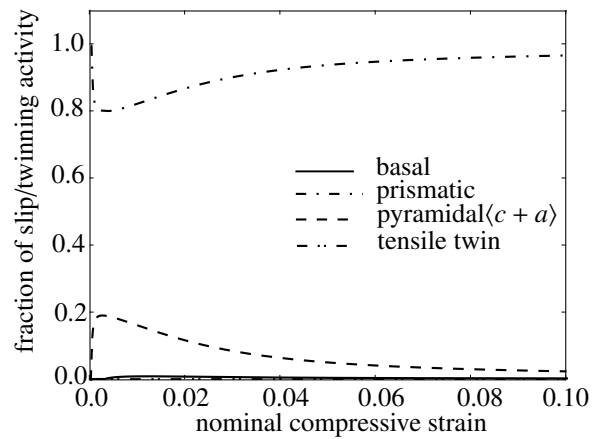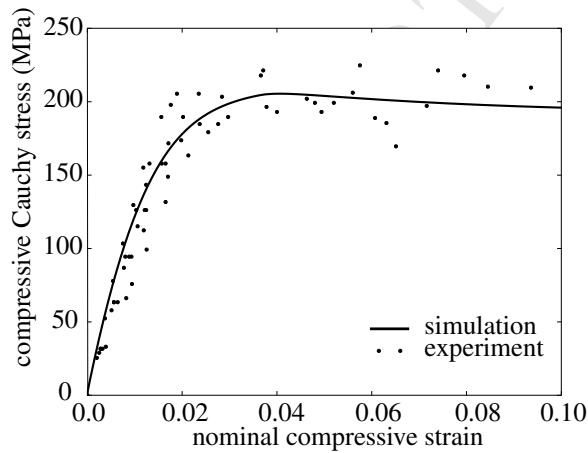
Case c: compression perpendicular to the constrained ⟨0001⟩-axis.

Figure 3: Numerical results for plane-strain compression compared to experimental data of (Kelley and Hosford, 1968b).

13
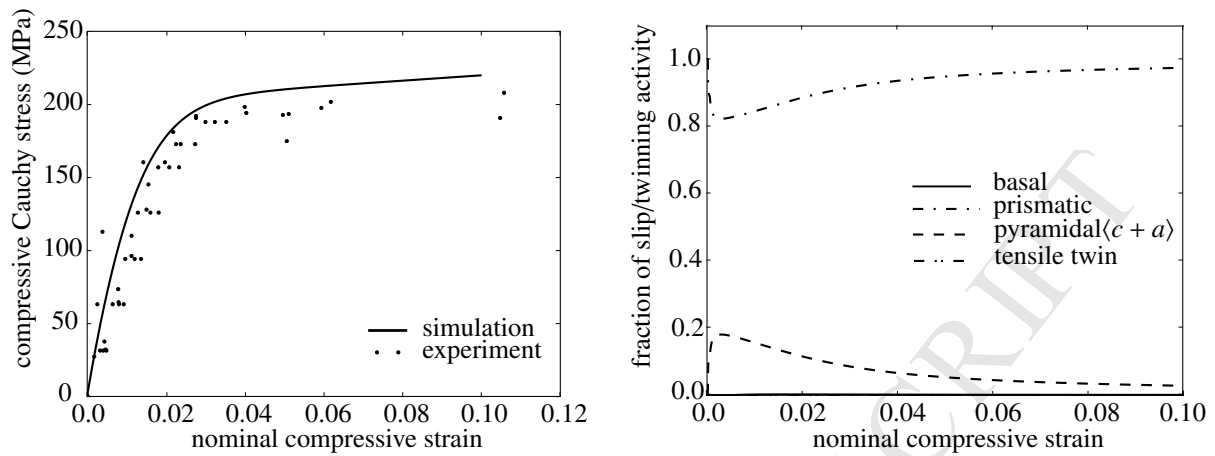
Case d: compression perpendicular to the constrained ⟨0001⟩-axis.
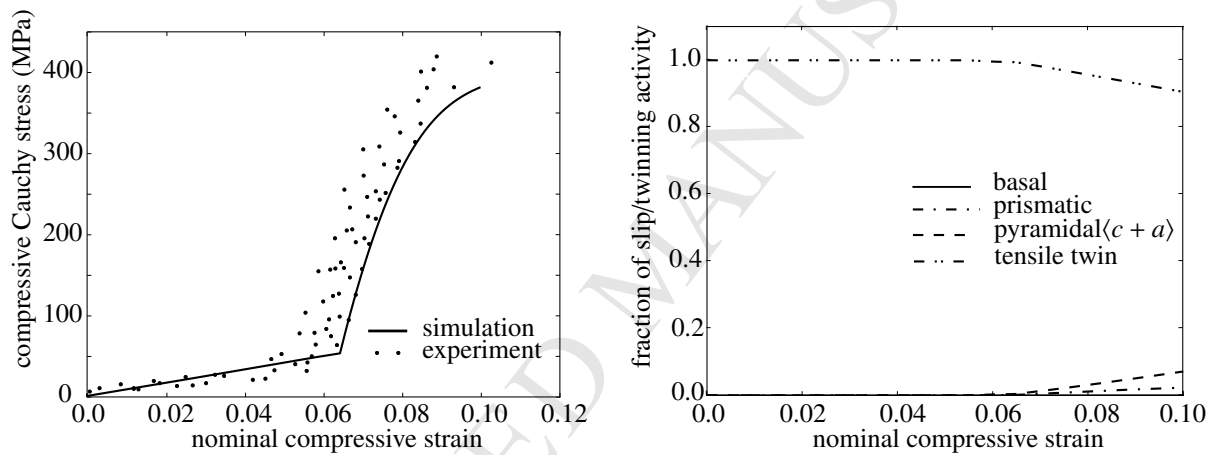
Case e: compression perpendicular to the unconstrained ⟨0001⟩-axis.
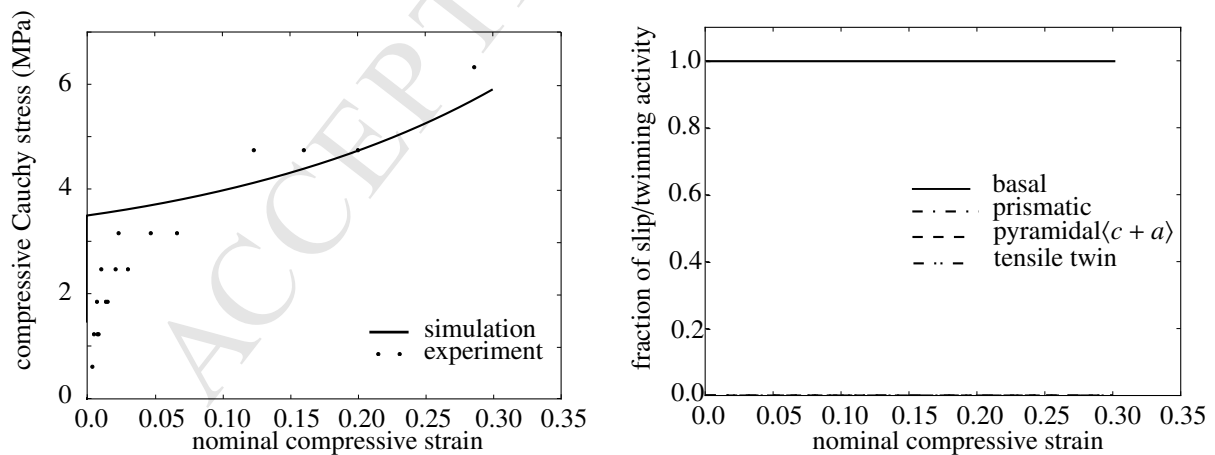
Case g: compression oriented for basal slip.

Figure 4: Numerical results for plane-strain compression compared to experimental data of (Kelley and Hosford, 1968b), continued.

14

in the early stages of deformation. Kelley and Hosford (1968b) explained this behavior by a small albeit sufficient misalignment of the sample orientation, which immediately leads to the activation of basal slip. In the ideally oriented scenario studied here, we use this case to identify the parameters of the pyramidal $\langle c+a\rangle$ system in the model. As seen in Figure 3, the stress-strain responses observed in both cases are qualitatively identical with a slightly higher stress level in case b. This agrees with experimental observations by Kelley and Hosford (1968b) and with previous simulated results by Zhang and Joshi (2012). For both cases, the pyramidal slip mode dominates with over 80% of all slip activity, whereas contributions from basal slip and tensile twinning are negligible. The rather small contributions of prismatic slip in the early stages of deformation are immediate results of the reorientation of the crystal undergoing pyramidal slip. Yet, since the resolved shear stress on the pyramidal systems is considerably higher, the prismatic slip activity drops gradually.

- **Compression perpendicular to the constrained $\langle 0001\rangle$-axis**:

  In loading cases c and d, compression is perpendicular to the $\langle 0001\rangle$-direction and the sample is constrained in the $\langle 0001\rangle$-direction, which is therefore oriented to produce prismatic slip. Kelley and Hosford (1968b) did not observe traces of prismatic slip, which they theorized to stem from early stages of prismatic slip prelude to the $\{10\bar{1}1\}$ banding. Our results in Figures 3 and 4 show that the stress-strain responses for these two cases are similar and that plastic deformation primarily stems from prismatic slip and small traces of pyramidal $\langle c + a\rangle$ slip (less than 10% beyond 4% of compression). Basal slip and tensile twinning are not activated in this case.

- **Compression perpendicular to the unconstrained $\langle 0001\rangle$-axis**:

  In case e, compression is perpendicular to the now unconstrained $\langle 0001\rangle$-axis, which is favorable to active the $\{10\bar{1}2\}$ tensile twin system. Kelley and Hosford (1968b) reported the completion of twinning at about 6% of compressive strain, which is followed by a similar behavior as compression along the $\langle 0001\rangle$-axis (see case a). This is consistent with our simulated results: tensile twinning is completed at about 6.5% compression. Since the $\langle 0001\rangle$-axis has reoriented by only about 4° with respect to the loading direction, we indeed see a similar behavior as in case a once the material is fully twinned. Figure 4 illustrates how twinning dominates the plastic deformation up to 6.5% compression, from where on we observe a combination of $\langle c + a\rangle$ pyramidal and prismatic slip as observed in experiments.

- **Compression resulting in basal slip**:

  Case g is favorable for basal $\{0001\}\langle 1\bar{2}10\rangle$ easy glide, and all plastic straining can be accommodated by a single basal slip system. In fact, Kelley and Hosford (1968b) reported significant basal band formation for this case. Our simulations predict that the stress remains at a rather low level (below 10 MPa) even at large strains (up to 30% of compression). Plastic deformation is exclusively accommodated by basal slip since no other system can operate at such low stress levels.

We note that we have omitted case f from our validation tests for the following reason. This loading scenario is similar to case e (i.e., loading is perpendicular to the unconstrained $\langle 0001\rangle$-axis) but the crystal is rotated by 90° about the $\langle 0001\rangle$-axis. As a consequence, the preferred deformation mode is tensile twinning followed by basal slip (Kelley and Hosford, 1968b). However, the tensile twin system involved in this case results in deformation in the 2-direction, which is suppressed by imposing deformation gradient (43) in our material point calculations. In experiments, the boundary conditions can be accommodated since the deformation is not uniform throughout the sample, which allows for stress relaxation by tensile twinning inside the specimen. Such behavior can be accounted for by boundary value calculations, see also (Zhang and Joshi, 2012). The compression twin is of only little relevance in our subsequent numerical examples; therefore, we assign the same parameters as for the tensile twin systems but with a significantly higher activation stress (hardening modulus $h_0 = 170$MPa). Similarly, pyramidal $\langle a\rangle$ slip could not be calibrated; where required in the following, we adopt those parameters obtained for pyramidal $\langle c + a\rangle$ slip due to a lack of validation data.

Overall, we observe a good quantitative agreement between the experimentally-determined and the numerically-computed stress-strain responses for six of the seven loading cases. In addition (and more importantly), we obtain excellent qualitative agreement between the experimentally-observed slip and twin activity and the simulated evolution of plastic slips and twin volume fractions.

15

loading scenario:	a	b	c	d	e	g
implicit updates:	$8.0 \cdot 10^{-4}$ (50)	$1.3 \cdot 10^{-3}$ (30)	$1.0 \cdot 10^{-3}$ (100)	$1.4 \cdot 10^{-3}$ (70)	$6.7 \cdot 10^{-4}$ (150)	$7.5 \cdot 10^{-5}$ (4000)
explicit updates:	$7.3 \cdot 10^{-6}$ (5500)	$7.8 \cdot 10^{-6}$ (5100)	$1.0 \cdot 10^{-5}$ (10000)	$9.0 \cdot 10^{-6}$ (11000)	NA (NA)	$1.5 \cdot 10^{-5}$ (20000)

(The above results are for $\tau_0 = 1.75$ MPa, the applied strain rate is 10^{-5}.)

loading scenario:	a	b	c	d	e	g
implicit updates:	$4.0 \cdot 10^{-3}$ (10)	$4.0 \cdot 10^{-3}$ (10)	$2.0 \cdot 10^{-3}$ (50)	$2.5 \cdot 10^{-3}$ (40)	$1.0 \cdot 10^{-3}$ (100)	$2.3 \cdot 10^{-4}$ (1300)
explicit updates:	$1.6 \cdot 10^{-5}$ (2500)	$1.5 \cdot 10^{-5}$ (2700)	$1.7 \cdot 10^{-5}$ (6000)	$2.0 \cdot 10^{-5}$ (5000)	NA (NA)	$2.0 \cdot 10^{-5}$ (15000)

(The above results are for $\tau_0 = 3.5$ MPa, the applied strain rate is 10^{-5}.)

loading scenario:	a	b	c	d	e	g
implicit updates:	$1.3 \cdot 10^{-3}$ (30)	$4 \cdot 10^{-3}$ (10)	$1.7 \cdot 10^{-3}$ (60)	$3.3 \cdot 10^{-3}$ (30)	$7.7 \cdot 10^{-4}$ (130)	$3.8 \cdot 10^{-4}$ (800)
explicit updates:	$1.0 \cdot 10^{-5}$ (4000)	$1.1 \cdot 10^{-5}$ (3800)	$1.4 \cdot 10^{-5}$ (7200)	$1.3 \cdot 10^{-5}$ (7500)	NA (NA)	$1.7 \cdot 10^{-5}$ (18000)

(The above results are for $\tau_0 = 1.75$ MPa, the applied strain rate is 10^{-2}.)

Table 5: Summary of the maximum strain increments suitable for the stable convergence of the implicit and explicit schemes (numbers in parentheses denote the corresponding minimum numbers of load steps) for different values of the slip dissipation parameter and for different strain rates, as determined by numerical experimenting.

4.2. Model efficiency and stability: comparison to explicit update models

Most available crystal plasticity-based models for slip-twinning interactions in Mg use explicit updates of the internal variables in contrast to the implicit, variational approach presented here. The latter possesses several advantages over the existing direct updates-based models which discretize the evolution equations (18) explicitly. As a consequence, such models commonly assume rate-dependent evolution laws for all internal variables, which is questionable for the evolution of twinning as discussed earlier, see e.g. (Ulacia et al., 2010) for the low rate sensitivity of Mg alloys. The present model handles both rate-dependent and rate-independent evolution laws (here, for the plastic slips and the twin volume fractions, respectively) in the same manner. We note that rate-independent plasticity has been modeled successfully through a variety of alternative approaches, including regularized models that remove yield surface singularities (Franciosi and Berbenni, 2007; Yoshida et al., 2009) or new time integration schemes (Schmidt-Baldassari, 2003). However, any explicit scheme requires small load increments and lacks convergence properties, whereas implicit schemes bring about numerical challenges such as the identification of the active set of slip and/or twin systems. For a discussion of rate independence within implicit plasticity modeling and associated challenges see e.g. (Kalidindi et al., 1992).

Our variational model admits the treatment of the evolution of the internal variables by both implicit and explicit updates. To demonstrate the advantages of the variational strategy, we have repeated the single-crystal simulations of Section 4.1 with the same model but using explicit updates comparable to conventional crystal plasticity-based models. For each simulation, we identify by numerical experimenting the minimum number of load steps required for the convergence of the variational approach (to less than 0.1% deviation of the stress-strain curve) as well as the minimum number of steps required for the stability of an explicit scheme (internal variables are updated explicitly upon each quasistatic equilibration). For each simulation, these along with the maximum applied strain can be translated into a maximum allowable strain increment. Results are summarized in Table 5 for different values of the slip dissipation parameters τ_0 in (35) and for different strain rates (note that the twinning-dominated case e is inconclusive since the rate-independent flow rule chosen here does not admit a direct treatment by explicit updates).

Fig. 5 illustrates the typical oscillatory solution obtained from the explicit scheme before instability. The plot shows results for case d of Section 4.1 simulated by using 7,000 and 5,000 load steps (with the maximum strain of

16

10% this correspond to shear strain increments of $1.4 \cdot 10^{-5}$ and $2 \cdot 10^{-5}$, respectively). Using fewer steps will cause the solver to show exponential instability within the first few load steps. For comparison, we plot the analogous results obtained from the implicit updates for 50 load steps in Fig. 6 on the right (which corresponds to strain increments of 0.2%). Similarly, Fig. 6 also illustrates implicit results for case a using only 10 load steps and producing convincing agreement with the exact solution obtained from very small strain increments. This confirms the stability and accuracy of the chosen implicit variational scheme at considerably larger steps, thus resulting in superior efficiency over comparable explicit schemes. The increased efficiency enables the investigation of larger samples, of more complex grain distributions, and of the homogenized material response, to name but a few examples.

Of course, the exact findings depend on the details of the chosen numerical algorithms but the general trend is apparent. The results in Table 5 show that the number of steps required for the variational approach are significantly (viz., on average a factor of 100) smaller than those of the explicit scheme. Note that we still need a fair amount of steps in order for several cases to converge, especially for easy-glide case g for basal slip. This, however, is purely a convergence issue arising from the employed Newton-Raphson solver.
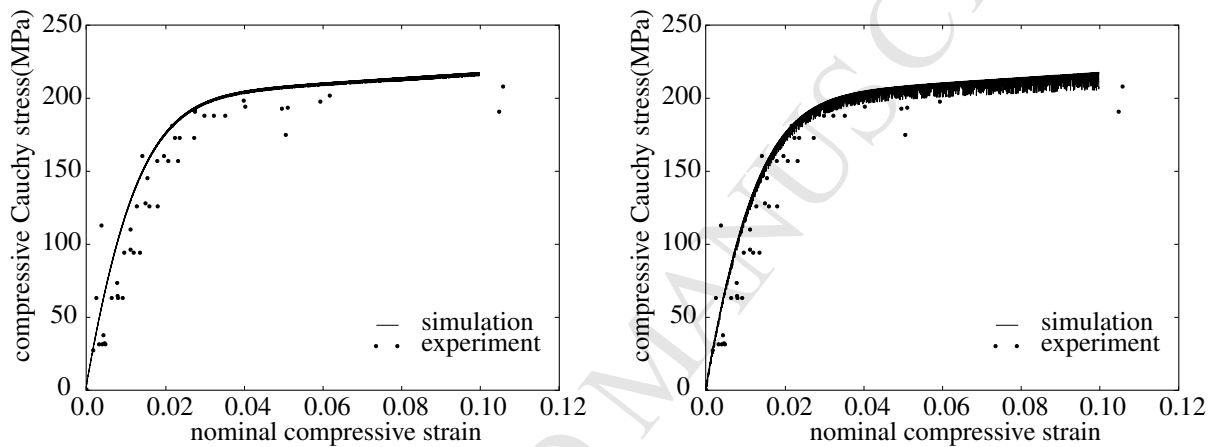

Figure 5: Results obtained by using explicit updates for case d of Section 4.1, computed via a total of 7000 load steps (left) and 5000 load steps (right) with $\tau_0 = 3.5$ MPa (i.e., simulations are run right at the stability limit).
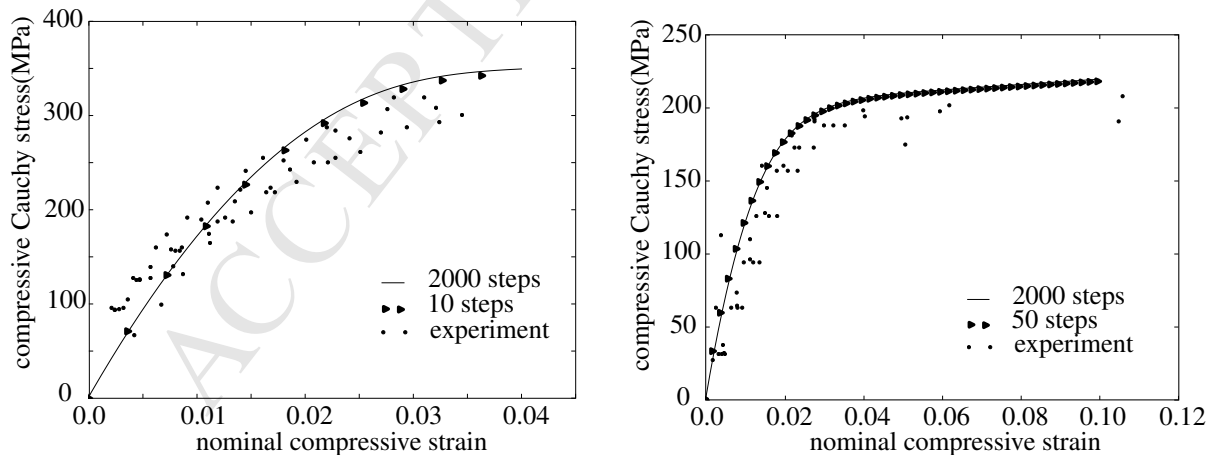

Figure 6: Results obtained by using implicit updates for cases a (left) and d (right) of Section 4.1, computed via a total of 10 load steps (left) and 50 load steps (right) and compared to the (approximately) exact solution obtained from a very fine load step in the implicit scheme (with a total of 2000 load steps); as before, $\tau_0 = 3.5$ MPa.

17

5. Simulation of polycrystalline texture evolution

Having validated the single-crystalline response of the variational model for each individual slip system, we proceed to exploit this model to study the collaborative effects of slip and twinning in polycrystalline Mg. This can be achieved in various ways with different levels of complexity. Here, we use two different approaches and compare their results (this will provide guidelines for their suitability). First, we use a Taylor-type model which does not account for grain interactions and grain boundary mechanisms but allows for the simulation of large numbers of grains, which will allow us to study polycrystalline texture evolution. The averaging scheme of Taylor (1938) assumes that each grain undergoes the same total (macroscopically-applied) deformation; it provides an upper bound on the stress-strain relation and has traditionally been used in texture calculations. For a polycrystal containing n_g grains with orientations defined by rotation tensors $\boldsymbol{R}_i \in SO(3)$, the total energy is assumed to be

$$W(\boldsymbol{F}) = \frac{1}{n_g} \sum_{i=1}^{n_g} W(\boldsymbol{R}_i \boldsymbol{F}) \tag{44}$$

and the energy of each grain is defined by (41). Stress and incremental modulus tensors follow accordingly. Since the Taylor assumption is too restrictive for certain microstructures to develop, we alternatively employ finite element simulations to determine the polycrystalline response. In close analogy to the single-crystal experiments studied above, Kelley and Hosford (1968a) also performed channel die tests on polycrystalline Mg. Here, a finite element simulation of a cubic block undergoing constrained compression is much more suitable than using the Taylor assumption since it admits the operation of slip/twin systems which are otherwise suppressed by the out-of-plane constraints. The spatial variation of deformation mechanisms within the specimen are modeled by linear tetrahedral elements (each quadrature point is assigned a different grain orientation) and the macroscopic response is obtained by imposing suitable boundary conditions.

5.1. Lattice reorientation due to slip and twinning

Changes of the lattice orientation during severe plastic deformation can be extracted from the evolution of the internal variables, as is commonly performed in the context of crystal plasticity, see e.g. (Asaro, 1983; Asaro and Needleman, 1985; Ahzi et al., 1993). Here, we follow a similar approach but with modifications to incorporate the reorientation effects due to twinning. Using (3), the plastic contribution to the rate of stretching tensor is given by

$$\dot{\boldsymbol{F}}\boldsymbol{F}^{-1} - \dot{\boldsymbol{F}}_e \boldsymbol{F}_e^{-1} = \boldsymbol{D}_{in} + \boldsymbol{\Omega}_{in} = \boldsymbol{F}_e \tilde{\boldsymbol{l}}_{in} \boldsymbol{F}_e^{-1}, \tag{45}$$

where $\boldsymbol{D}_{in}$ and $\boldsymbol{\Omega}_{in}$ are the symmetric and antisymmetric parts of the inelastic velocity gradient, defining the stretching rate and the spin tensor of the inelastic deformation. The total rates of the stretch and spin tensors decompose additively into their elastic and inelastic parts, i.e.

$$\boldsymbol{D} = \boldsymbol{D}_e + \boldsymbol{D}_{in}, \qquad \boldsymbol{\Omega} = \boldsymbol{\Omega}_e + \boldsymbol{\Omega}_{in}, \tag{46}$$

where $\boldsymbol{D}$ and $\boldsymbol{\Omega}$ correspond to the stretching rate and spin tensor of the total deformation, respectively. Since the lattice structure is assumed to remain unaffected by plastic deformation, the reorientation is governed by the elastic spin tensor $\boldsymbol{\Omega}_e = \boldsymbol{\Omega} - \boldsymbol{\Omega}_{in}$, which we use to obtain the lattice rate of rotation, i.e. the rate of rotation of the c-axis (represented by unit vector $\boldsymbol{c}$):

$$\dot{\boldsymbol{c}} = \boldsymbol{\Omega}_e \, \boldsymbol{c}, \tag{47}$$

In incremental form this results in

$$\boldsymbol{c}(t^{n+1}) = \exp(\boldsymbol{\Omega}_e \Delta t) \, \boldsymbol{c}(t^n). \tag{48}$$

Twinning affects the lattice orientation by a reflection about the twin plane, which can have a significant effect on the texture evolution in polycrystals (Clausen et al., 2008) and is therefore accounted for. As discussed in Section 3.3, we only allow one twin system to operate at a time. Consequently, we apply the corresponding lattice reflection as soon as one of the twin volume fractions λ_β exceeds a system-specific threshold, i.e.,

$$\boldsymbol{c}(t^{n+1}) = \boldsymbol{Q}_\beta \, \boldsymbol{c}(t^n) \qquad \text{if} \quad \lambda_\beta(t^n) < \lambda_{cr,\beta}, \quad \text{and} \quad \lambda_\beta(t^{n+1}) > \lambda_{cr,\beta}, \tag{49}$$

18

where $\boldsymbol{Q}_\beta$ is the reflection tensor of twin system β as defined in (5). The values of $\lambda_{\mathrm{cr},\beta}$ represent the physical thresholds at which the crystal may be regarded as being in a fully-twinned orientation. In the following numerical examples, we use $\lambda_{\mathrm{cr},\beta} = 0.8$ (the exact numerical value has only a limited influence on the simulated final results since it only affects the postprocessing of the simulated internal variable evolution).

5.2. Polycrystalline Mg – comparison with experiments

Kelley and Hosford (1968a) performed compression experiments on polycrystalline Mg, whose general setup is identical to that used for our single-crystalline simulations in Section 4.1. In their experiments, the polycrystalline Mg samples were obtained from cold rolling, which implies an initial texture with basal poles closely aligned with the rolling normal direction (ND). Here, we adopt the notation of Kelley and Hosford (1968a): each plane-strain compression test is characterized by two letters, the first denoting the axis of compression and the second one denoting the unconstrained axis. Thereby, the orientations in the cold-rolled samples are defined by the normal direction (ND, denoted by z), the rolling direction (RD, abbreviated as r), and the transverse direction (TD, t). As two selected examples, we demonstrate the performance of our model by simulating the responses of cases zt and rt and comparing to the experimental data using both a finite element model and the Taylor model. Both models start with initial grain distributions whose basal poles are closely aligned with the rolling ND, as shown in Figure 7. Experiments may be expected to have exhibited a spread of the initial textures as well. Numerical results for both loading cases are summarized in Figure 8. Because of the constraints in the Taylor model (and because of its efficiency), we simulate more grains (here, a total of 100) than in FE calculations (where only 24 grains appear sufficient). Results in Figure 8 indicate that both models predict similar stress-strain responses (with a slightly better qualitative agreement of the finite element results). The relative contributions of the slip/twin systems (also shown in the figure) are almost identical in the Taylor and FE models, which is why we only show results obtained from the Taylor approach.

- In **case** zt, the loading direction is aligned with the ND while the TD is unconstrained. The initial texture is assumed to have a wider spread than in case rt, cf. Figure 7. This is reasonable since the experimentally-determined stress level of Kelley and Hosford (1968a) for this case is low (around 200 MPa) compared to the single-crystal compression cases a and b in Section 4.1 (stress levels were near 300 MPa). Hence, a fair amount of basal activity is required to reduce the stress. The results obtained from FE calculations and from the Taylor model are quite similar both in the stress-strain response and in the relative contributions of the different slip/twin systems. Unlike in the single-crystal cases in Section 4.1, not a single slip system dominates the process but all slip modes are activated, combining basal, prismatic, and pyramidal $\langle c + a \rangle$ slips. In contrast, tensile twinning appears less pronounced.

- In **case** rt, the loading direction coincides with the RD and the TD remains unconstrained. The results from FE calculations and from the Taylor model again agree fairly well. The dominant deformation mode in both cases is prismatic slip like in single-crystal cases c and d in Section 4.1. We also see a small amount of tensile twinning at low strains, which results from the spreading of basal poles around the ND.

(a) initial textures used in the Taylor model (b) initial textures used in FE simulations
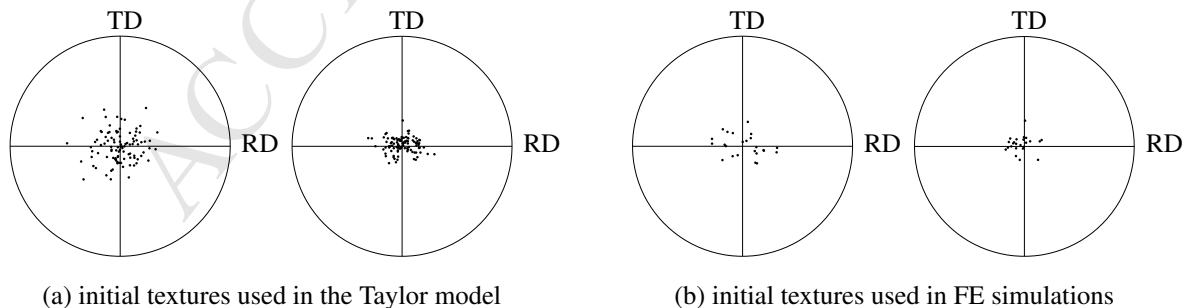
Figure 7: Initial textures used for polycrystalline Mg samples for plane-strain compression tests (total of 100 grains for the Taylor model and a reduced set of 24 grains for FE simulations); shown are (0001)-poles aligned with the ND. Left and right pole figures in both (a) and (b) are for cases loading cases zt and rt, respectively.
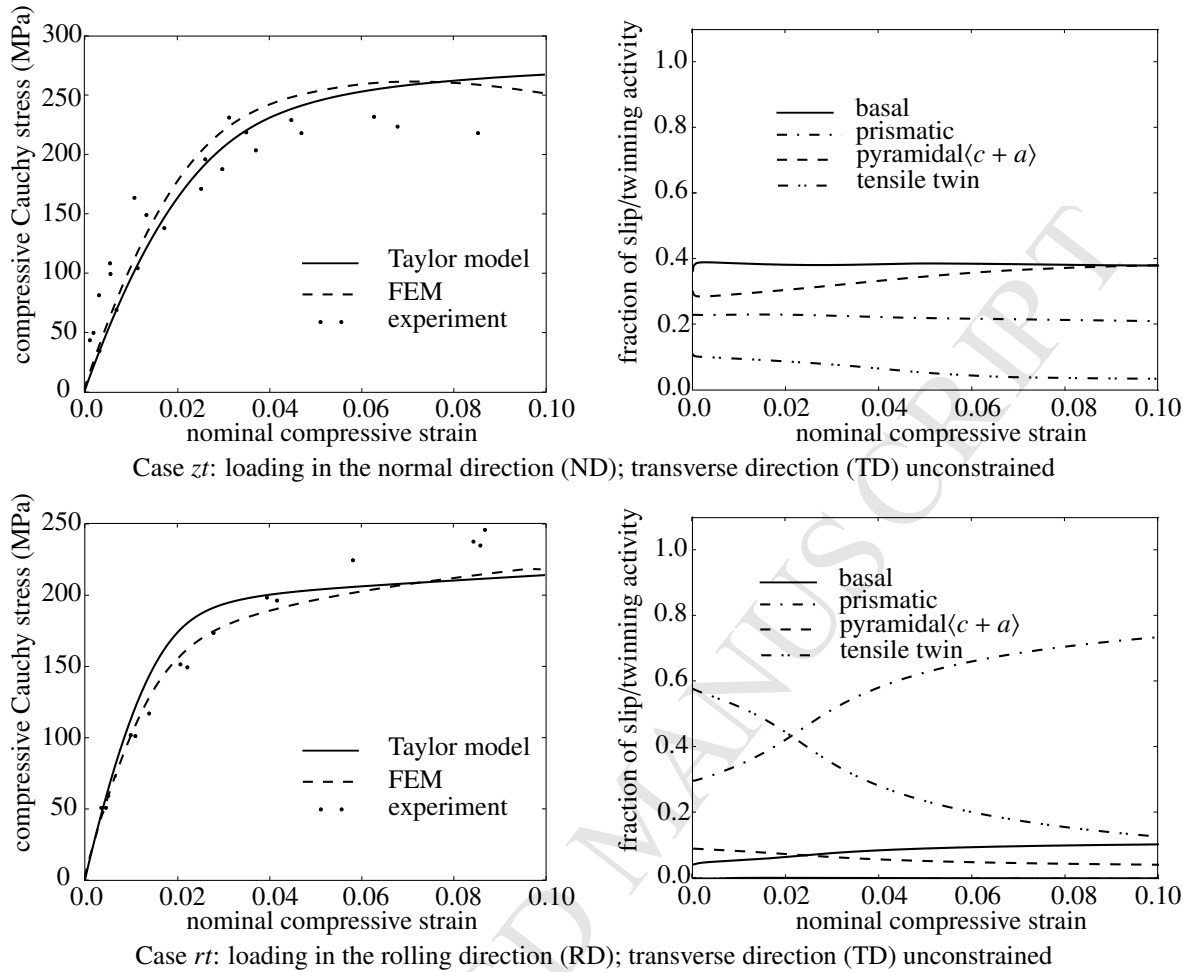
19

Figure 8: Numerical results for plane-strain compression of Mg polycrystals compared to experimental data of (Kelley and Hosford, 1968a). Shown are the stress-strain responses as well as the relative contributions of all slip/twin modes.

It is important to note that we compare numerical stress-strain predictions (without having fitted the model to any polycrystalline data) to independent polycrystalline experimental results. Both experiments and simulations contain numerous potential error sources which may lead to the discrepancies between the simulated results and the experimental data, including the following. The texture evolution depends significantly on the initial texture and on the loading history. Like in almost all computational approaches, our simulations start with a specific initial texture which mimics the experimental reality but cannot agree exactly with the physical microstructure, among others due to limited resolution and computational costs. Furthermore, we assume a textured but virgin state of the material; i.e., although an initial texture is accounted for, we assume that the internal variables display no hardening history. This is, of course, not the case in experiments, since the textured sample was produced by large plastic deformation. Unfortunately, there is no (simple) way to infer the exact amounts of preexisting plastic slips in the initial sample (and no such data are available). In addition, as explained in section 4.1, the only way to identify the model parameters for pyramidal $\langle c + a \rangle$ slip is through experimental data for c-axis compression, which is consistent with the approaches of e.g. Homayonifar and Mosler (2011, 2012); Zhang and Joshi (2012). However, this loading scenario is prone to produce small amounts of basal slip due to sample misalignment. Thus, a further error source arises from the difficulty in cleanly isolating the individual slip and twin modes in experiments. In summary, various potential error sources exist, which are hard to account for in simulations. However, considering that the results were produced without fitting the model to polycrystalline data (and considering that the model is the first variational model of its type), the comparison
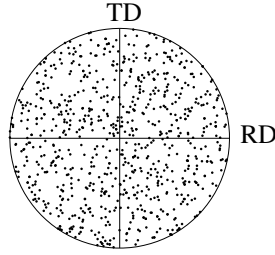
20

Figure 9: Initial texture distribution showing (0001)-poles are randomly-oriented at the beginning of each cold rolling simulation (with total of 800 grains)

of the experimental and simulated responses shown in our simulation are convincing.

5.3. Cold rolling example

Cold rolling is a common metal forming process that results in pronounced texture evolution. Experimental evidence indicates that plastic deformation during cold rolling primarily leads to the alignment of basal planes with the rolling direction (RD) with increasing deformation (Sandlöbes et al., 2011). As pointed out e.g. by Lee and Duggan (1991), the deformation during the rolling process is characterized by superimposed shear and compressive strains. Following Ahzi et al. (1993), we simulate the effect of cold rolling by imposing a total velocity gradient $\boldsymbol{l}$ that contains both shear (with rate $\dot{\gamma}$) and plane-strain tension-compression (with rate $\dot{\varepsilon}$) according to

$$\boldsymbol{l} = \begin{bmatrix} \dot{\varepsilon} & 0 & \dot{\gamma} \\ 0 & 0 & 0 \\ 0 & 0 & -\dot{\varepsilon} \end{bmatrix}. \tag{50}$$

Here, the three coordinate directions (1, 2, and 3) correspond to the rolling direction (RD), the transverse direction (TD), and the normal direction (ND), respectively. The shear to normal strain rate ratio

$$\alpha = \dot{\gamma}/\dot{\varepsilon}, \tag{51}$$

is a characteristic property of the geometry of the rolling device. Here and in the following, we take $\alpha = 3$ to account for the fact that shear deformation dominates the rolling process, cf. (Ahzi et al., 1993) for a discussion. When starting from the virgin state of the material at time $t = 0$, the velocity gradient (50) can be integrated analytically, which leads to the volume-preserving total deformation gradient

$$\boldsymbol{F}(t) = \begin{bmatrix} e^{\dot{\varepsilon}t} & 0 & \dot{\gamma}t \\ 0 & 1 & 0 \\ 0 & 0 & e^{-\dot{\varepsilon}t} \end{bmatrix}. \tag{52}$$

Consequently, for an initial thickness H of a sample being rolled to thickness h, the relative thickness reduction during the rolling process follows as

$$\Delta H/H = (H - h)/H = 1 - e^{-\dot{\varepsilon}t}. \tag{53}$$

As discussed in Section 3.2, the complexity of the lattice structure of Mg is oftentimes described by only a reduced set of slip and twin systems, whose choice may lead to different material behavior. Here, we demonstrate the importance of an appropriate choice of the relevant systems by studying texture evolution in polycrystalline Mg, specifically accounting for

  i) basal, prismatic, and pyramidal $\langle a \rangle$ slip systems and $\{10\overline{1}2\}\langle\overline{1}011\rangle$ tensile twin systems.

  ii) basal, prismatic, and pyramidal $\langle c + a \rangle$ slip systems and $\{10\overline{1}2\}\langle\overline{1}011\rangle$ tensile twin systems.

  iii) basal, prismatic, and pyramidal $\langle a \rangle$ slip systems and $\{10\overline{1}1\}\langle\overline{1}012\rangle$ compression twin systems.
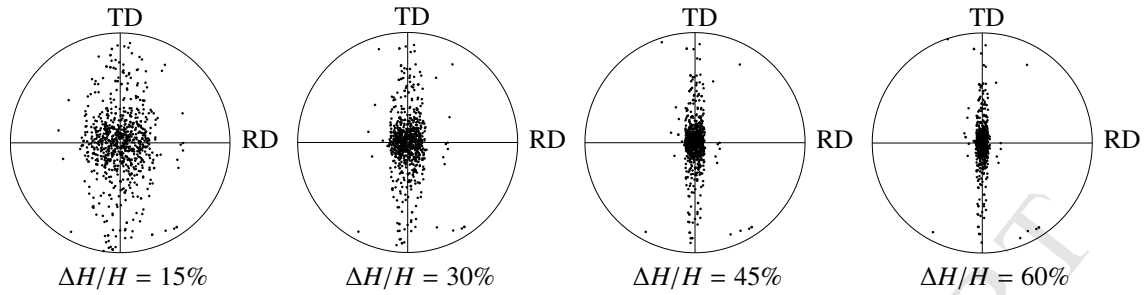
21

Figure 10: Case i: texture evolution during the cold rolling process, showing (0001)-poles moving towards the ND.
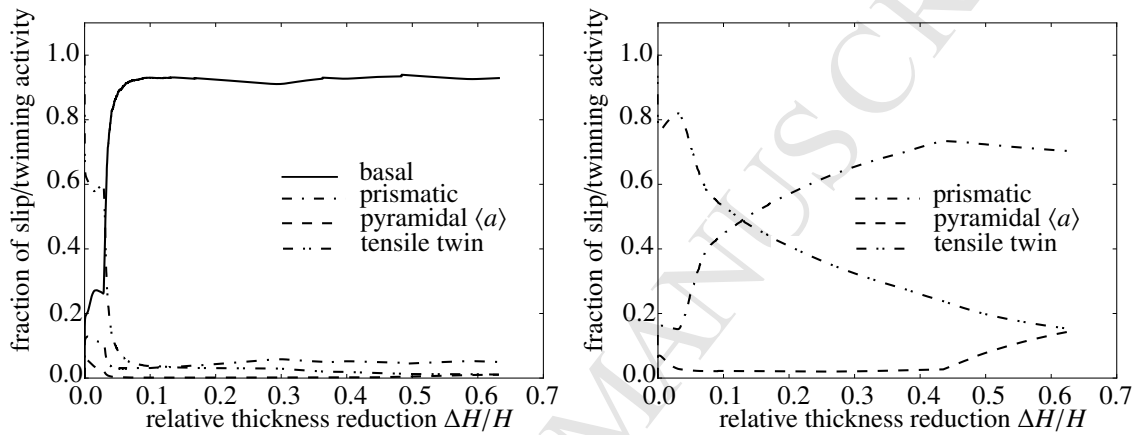

Figure 11: Case i: relative contributions of slip and twin systems to the response shown in Figure 10. The left figure shows all slip/twin system contributions; the right figure shows the contributions without the dominant basal slip.

For each case, Taylor-type simulations contain 800 initially randomly-oriented grains without pre-texture, as shown in the (0001)-pole figure in Figure 9 (each dot in the figure denotes an individual grain). We apply a constant strain rate of $\dot{\varepsilon} = 1 \times 10^{-5}$. The resulting grain distribution for each of the three cases at thickness reductions of $\Delta H/H = 15\%$, 30%, 45% and 60% is illustrated by (0001)-pole figures as well as the fraction of relative slip-twin activity during the process. Since basal slip dominates with more than 90% of all plastic activity, we also show the relative activity of the remaining slip/twin systems excluding basal slip.

- **case i: pyramidal $\langle a \rangle$ slip systems are included while pyramidal $\langle c + a \rangle$ slip systems are not included**

  Pyramidal $\langle c + a \rangle$ slip has been rarely observed during cold rolling, which is why we include the pyramidal $\langle a \rangle$ systems rather than pyramidal $\langle c + a \rangle$ slip. Figure 10 illustrates the resulting grain distributions with increasing levels of thickness reduction. Figure 11 shows the relative activities of each slip/twin system. Obviously, the (0001)-poles gradually move towards the rolling ND, which is mainly due to activity on the basal slip systems (more than 90% of the total slip is basal). Note that the alignment of the grain orientations in the rolling direction is considerably faster than in the transverse direction. This can be explained by the direction of the applied simple shear. In technological applications, typical cold rolling procedures often involve several passes of a single work piece through the rolling device, and each pass can be performed with a different rolling direction, which ultimately leads to a faster directional alignment. It is important to note that, although the overall plastic deformation of the polycrystal is mainly the result of basal slip activity, we do observe a significant number of grains undergoing tensile twinning at low deformation levels. At small thickness reductions of $\Delta H/H < 7\%$ more than 60% of the total plastic deformation comes from twinning, see Figure 11. However, as those grains approach the twinned states, basal slip activity in the twinned grains catches up and dominates the ensuing deformation.
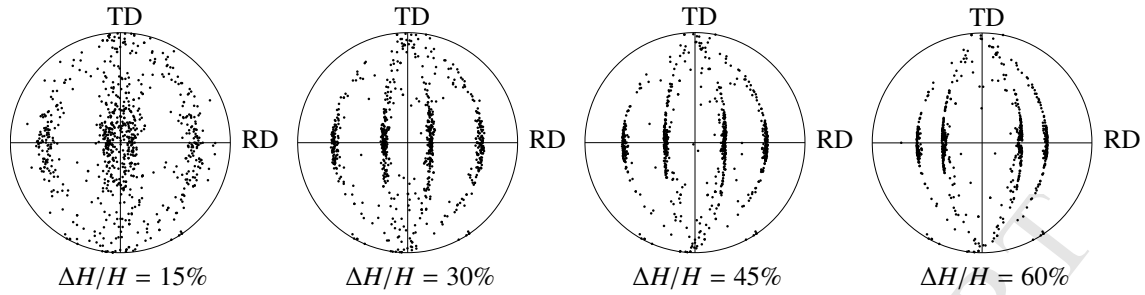
22

Figure 12: Case ii: texture evolution during the cold rolling process shown by (0001)-pole figures.
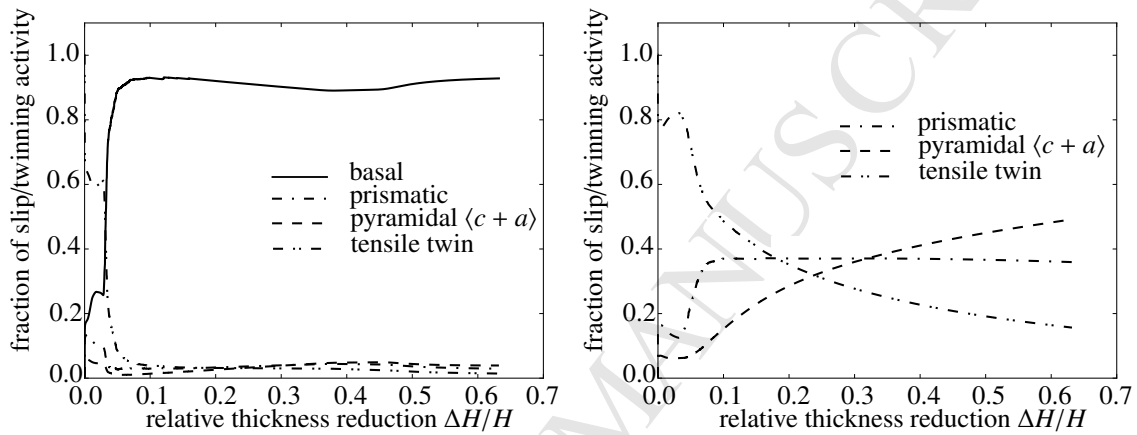

Figure 13: Case ii: relative contributions of slip and twin systems to the response shown in Figure 12. The left figure shows all slip/twin system contributions; the right figure shows the contributions without the dominant basal slip.

- **case ii: pyramidal $\langle c + a \rangle$ slip systems are included while pyramidal $\langle a \rangle$ slip systems are not included**

  Most models in the literature have included pyramidal $\langle c + a \rangle$ systems (like we did in Section 4.1) to accommodate non-basal slip. For this case, the grain distribution and the relative activity of each slip/twin system for the same cold rolling scenario are summarized in Figures 12 and 13, respectively. Here, we observe a quite different texture evolution compared to the previous case. Indeed, the final grain distribution resembles that of plane-strain compression of fcc metals, see e.g. (Wang et al., 2010). The activation of the pyramidal $\langle c + a \rangle$ systems tends to reorient the basal slip systems. Although the overall deformation is dominated by basal activity, the contributions of the pyramidal slip systems (the dashed line in Figure 13) are significantly higher than in the previous case.

- **case iii: compression twin systems are included while tensile twin systems are not included**

  Because of the high critical resolved shear stress and large critical shear strain, compression twins are rarely observed and often omitted in simulated texture predictions, see e.g. (Proust et al., 2009; Homayonifar and Mosler, 2011). For illustrative purposes, we include compression twinning (and suppress tensile twinning) to demonstrate its effect on the texture evolution. Grain distribution and relative slip/twin activities for this case are shown in Figures 14 and 15, respectively. The polycrystal does not develop any preferably-oriented texture in this case because of the high barrier to activate compression twins. Figure 16 plots the average volume fractions of tensile twins in case i) and of compression twins in this case across all grains. In case i), the averaged twin volume fractions reach 50% at about 15% of thickness reduction and remain at this level because almost 50% of all grains exhibit tensile twinning. There, due to the low critical shear strain of tensile twinning, after around 15% of thickness reduction nearly all grains that undergo twinning are fully in the twinned orientation
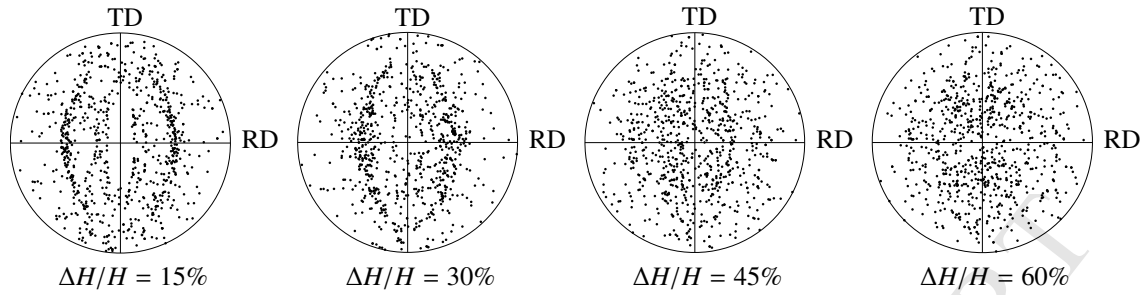
23

Figure 14: Case iii: texture evolution during the cold rolling process shown by (0001)-pole figures.
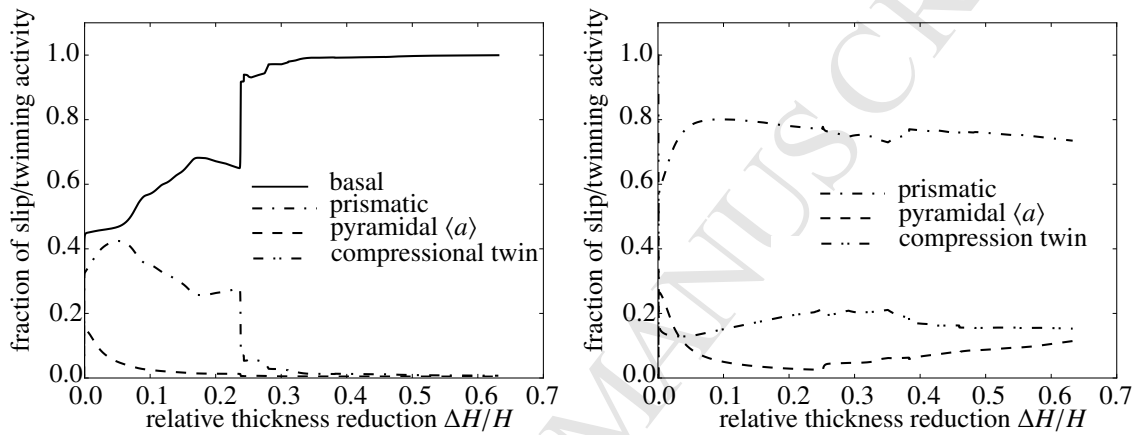

Figure 15: Case iii: relative contributions of slip and twin systems to the response shown in Figure 14. The left figure shows all slip/twin system contributions; the right figure shows the contributions without the dominant basal slip.

and basal slip proceeds to dominate almost all plastic deformation for grains both in the parent and in the twinned orientation. Here, in contrast, compression twins are hard to activate and difficult to complete. When they are the only means to accomodate deformation along the $\langle 0001 \rangle$-axis, we see the average twin volume fractions remain at a very low level and only increase at large strains. As a consequence, grains will update their orientation even at large strains because of the lattice reorientation due to twinning, which is why the Mg polycrystal is unlikely to develop texture preferences, as seen in Figure 14.

In summary, texture development in Mg polycrystals during cold rolling have been simulated by the presented variational model. Basal pole alignment with the normal direction, as frequently seen in experiments on both pure and alloyed Mg (Bohlen et al., 2007; Al-Maharbi et al., 2011; Sandlöbes et al., 2011), can only be predicted without including the pyramidal $\langle c + a \rangle$ slip systems in the Taylor-type model, which is an important observation. No texture development is observed when including the compression twin systems as the only non-basal relaxation scheme because of the high critical resolved shear stress and critical twin volume fraction of the compression twin systems.

6. Conclusions

We have presented a relatively simple variational model to describe the effective mechanical response of hcp metals and particularly of pure Mg single- and polycrystals, whose inelastic performance is governed by the interplay of slip and twinning. Using variational constitutive updates, we employed an extended crystal plasticity model to include deformation twinning and the associated lattice reorientations. The specifics of basal, pyramidal, and prismatic slip as well as of the tensile and compressive twin systems are described by the respective representations of stored inelastic work and of the dissipation potential. The elastic anisotropy of the hcp crystallography is modeled by a polyconvex
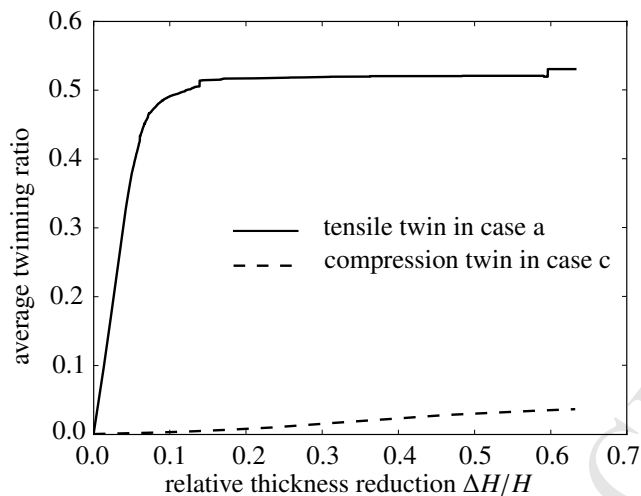
24

Figure 16: Comparison of the average twin volume fractions across all grains for cases i) and iii).

strain energy density. The model has been validated and material parameters determined by a direct comparison to experimental data for single- and polycrystalline Mg, showing good quantitative and qualitative agreement and superior efficiency compared to modeling approaches based on explicit updates of the internal variables. The model was further exploited to predict the texture evolution of polycrystalline Mg during cold rolling. Owing to its variational structure, the presented model allows for various extensions including, but not limited to, thermo-mechanical coupling and high strain rate – research in these directions is underway and will be reported elsewhere. Of course, like every macroscopic continuum model, the presented approach is based on a number of simplifying assumptions which greatly affect the balance between accuracy and efficiency and which may be refined in the future.

Acknowledgments

References

Agnew, Tomé, C. N., Brown, D. W., Holden, T. M., Vogel, S. C., 2003. Study of slip mechanisms in a magnesium alloy by neutron diffraction and modeling. Scripta Materialia 48 (8), 1003 – 1008.
URL http://www.sciencedirect.com/science/article/pii/S1359646202005912

Agnew, S., Brown, D., Tomé, C., 2006. Validating a polycrystal model for the elastoplastic response of magnesium alloy {AZ31} using in situ neutron diffraction. Acta Materialia 54 (18), 4841 – 4852.
URL http://www.sciencedirect.com/science/article/pii/S1359645406004502

Agnew, S., Yoo, M., Tomé, C., 2001. Application of texture simulation to understanding mechanical behavior of mg and solid solution alloys containing li or y. Acta Materialia 49 (20), 4277 – 4289.
URL http://www.sciencedirect.com/science/article/pii/S135964540100297X

Agnew, S. R., Duygulu, Ö., 2005. Plastic anisotropy and the role of non-basal slip in magnesium alloy {AZ31B}. International Journal of Plasticity 21 (6), 1161 – 1193, plasticity of Multiphase Materials.
URL http://www.sciencedirect.com/science/article/pii/S0749641904001408

Ahzi, S., Asaro, R. J., Parks, D. M., 1993. Application of crystal plasticity theory for mechanically processed {BSCCO} superconductors. Mechanics of Materials 15 (3), 201 – 222.
URL http://www.sciencedirect.com/science/article/pii/016766369390018M

Al-Maharbi, M., Karaman, I., Beyerlein, I. J., Foley, D., Hartwig, K. T., Kecskes, L. J., Mathaudhu, S. N., 2011. Microstructure, crystallographic texture, and plastic anisotropy evolution in an mg alloy during equal channel angular extrusion processing. Materials Science and Engineering:

25

A 528 (25-26), 7616 – 7627.

URL http://www.sciencedirect.com/science/article/pii/S0921509311007106

Ando, S., Tonda, H., 2000. Non-basal slip in magnesium-lithium alloy single crystals. Materials Transactions, JIM(Japan) 41 (9), 1188–1191.

Arsenlis, A., Parks, D. M., 2002. Modeling the evolution of crystallographic dislocation density in crystal plasticity. Journal of the Mechanics and Physics of Solids 50 (9), 1979 – 2009.

URL http://www.sciencedirect.com/science/article/pii/S002250960100134X

Asaro, R., Needleman, A., 1985. Overview no. 42 texture development and strain hardening in rate dependent polycrystals. Acta Metallurgica 33 (6), 923 – 953.

URL http://www.sciencedirect.com/science/article/pii/0001616085901889

Asaro, R., Rice, J., 1977. Strain localization in ductile single crystals. Journal of the Mechanics and Physics of Solids 25 (5), 309 – 338.

URL http://www.sciencedirect.com/science/article/pii/0022509677900011

Asaro, R. J., 1983. Crystal plasticity. Journal of Applied Mechanics 50, 921–934.

URL http://dx.doi.org/10.1115/1.3167205

Avedesian, M., Baker, H., 1999. Magnesium and Magnesium Alloys. ASM SpecialtyHandbook. ASM International.

Ball, E., Prangnell, P., 1994. Tensile-compressive yield asymmetries in high strength wrought magnesium alloys. Scripta Metallurgica et Materialia 31 (2), 111 – 116.

URL http://www.sciencedirect.com/science/article/pii/0956716X94901597

Ball, J., James, R., 1987. Fine phase mixtures as minimizers of energy. Archive for Rational Mechanics and Analysis 100 (1), 13–52.

URL http://dx.doi.org/10.1007/BF00281246

Ball, J. M., 1976. Convexity conditions and existence theorems in nonlinear elasticity. Archive for Rational Mechanics and Analysis 63, 337–403, 10.1007/BF00279992.

URL http://dx.doi.org/10.1007/BF00279992

Barnett, M., 2007. Twinning and the ductility of magnesium alloys: Part ii. Ž01ccontractionŽ01d twins. Materials Science and Engineering: A 464 (1-2), 8 – 16.

URL http://www.sciencedirect.com/science/article/pii/S0921509307004297

Bertin, N., Capolungo, L., Beyerlein, I., 2013. Hybrid dislocation dynamics based strain hardening constitutive model. International Journal of Plasticity 49 (0), 119 – 144.

URL http://www.sciencedirect.com/science/article/pii/S0749641913000739

Bohlen, J., Nuernberg, M. R., Senn, J. W., Letzig, D., Agnew, S. R., 2007. The texture and anisotropy of magnesium-zinc-rare earth alloy sheets. Acta Materialia 55 (6), 2101 – 2112.

URL http://www.sciencedirect.com/science/article/pii/S1359645406008214

Brown, D., Agnew, S., Bourke, M., Holden, T., Vogel, S., Tomé, C., 2005. Internal strain and texture evolution during deformation twinning in magnesium. Materials Science and Engineering: A 399 (1-2), 1 – 12, measurement and Interpretation of Internal/Residual Stresses.

URL http://www.sciencedirect.com/science/article/pii/S0921509305001541

Burke, E., Hibbard, W., 1952. Plastic deformation of magnesium single crystals. Transactions of the Metallurgical Society of AIME 194, 295–303.

Carstensen, C., Hackl, K., Mielke, A., 2002. Non-convex potentials and microstructures in finite-strain plasticity. Proc. R. Soc. London, Ser. A 458 (2018), 299–317.

Chapuis, A., Driver, J. H., 2011. Temperature dependency of slip and twinning in plane strain compressed magnesium single crystals. Acta Materialia 59 (5), 1986 – 1994.

URL http://www.sciencedirect.com/science/article/pii/S1359645410008190

Christian, J., Mahajan, S., 1995. Deformation twinning. Progress in Materials Science 39 (1-2), 1 – 157.

URL http://www.sciencedirect.com/science/article/pii/0079642594000077

Chun, Y., Davies, C., 2011. Twinning-induced negative strain rate sensitivity in wrought mg alloy {AZ31}. Materials Science and Engineering: A 528 (18), 5713 – 5722.

URL http://www.sciencedirect.com/science/article/pii/S0921509311004916

Clausen, B., Tomé, C., Brown, D., Agnew, S., 2008. Reorientation and stress relaxation due to twinning: Modeling and experimental characterization for mg. Acta Materialia 56 (11), 2456 – 2468.

URL http://www.sciencedirect.com/science/article/pii/S1359645408000724

Clayton, J., Knap, J., 2011. A phase field model of deformation twinning: Nonlinear theory and numerical simulations. Physica D: Nonlinear Phenomena 240 (9Ž01310), 841 – 858.

URL http://www.sciencedirect.com/science/article/pii/S0167278910003623

Clayton, J., Knap, J., 2013. Phase-field analysis of fracture-induced twinning in single crystals. Acta Materialia 61 (14), 5341 – 5353.

URL http://www.sciencedirect.com/science/article/pii/S1359645413003911

Comi, C., Corigliano, A., Maier, G., 1991. Extremum properties of finite-step solutions in elastoplasticity with nonlinear mixed hardening. International Journal of Solids and Structures 27 (8), 965 – 981.

URL http://www.sciencedirect.com/science/article/pii/002076839190094V

Comi, C., Maier, G., Perego, U., 1992. Generalized variable finite element modeling and extremum theorems in stepwise holonomic elastoplasticity with internal variables. Computer Methods in Applied Mechanics and Engineering 96 (2), 213 – 237.

URL http://www.sciencedirect.com/science/article/pii/0045782592901335

Conti, S., Ortiz, M., 2008. Minimum principles for the trajectories of systems governed by rate problems. Journal of the Mechanics and Physics of Solids 56 (5), 1885 – 1904.

URL http://www.sciencedirect.com/science/article/pii/S0022509607002220

Conti, S., Theil, F., 2005. Single-slip elastoplastic microstructures. Archive for Rational Mechanics and Analysis 178 (1), 125–148.

URL http://dx.doi.org/10.1007/s00205-005-0371-8

Franciosi, P., Berbenni, S., 2007. Heterogeneous crystal and poly-crystal plasticity modeling from a transformation field analysis within a regular-

26

ized schmid law. Journal of the Mechanics and Physics of Solids 55 (11), 2265 – 2299.
URL http://www.sciencedirect.com/science/article/pii/S0022509607000865

Glüge, R., Bertram, A., Böhlke, T., Specht, E., 2010. A pseudoelastic model for mechanical twinning on the microscale. ZAMM - Journal of Applied Mathematics and Mechanics / Zeitschrift fr Angewandte Mathematik und Mechanik 90 (7-8), 565–594.
URL http://dx.doi.org/10.1002/zamm.200900339

Graff, S., Brocks, W., Steglich, D., 2007. Yielding of magnesium: From single crystal to polycrystalline aggregates. International Journal of Plasticity 23 (12), 1957 – 1978.
URL http://www.sciencedirect.com/science/article/pii/S0749641907001076

Hackl, K., Fischer, F. D., 2008. On the relation between the principle of maximum dissipation and inelastic evolution given by dissipation potentials. Proceedings of the Royal Society A: Mathematical, Physical and Engineering Science 464 (2089), 117–132.

Hansen, B., Beyerlein, I., Bronkhorst, C., Cerreta, E., Dennis-Koller, D., 2013. A dislocation-based multi-rate single crystal plasticity model. International Journal of Plasticity 44 (0), 129 – 146.
URL http://www.sciencedirect.com/science/article/pii/S0749641912001957

Hauser, F., Landon, P., Dorn, J., 1956. Deformation and fracture mechanisms of polycrystalline magnesium at low temperatures. Trans. ASM 48, 986–1002.

Hill, R., 1966. Generalized constitutive relations for incremental deformation of metal crystals by multislip. Journal of the Mechanics and Physics of Solids 14 (2), 95 – 102.
URL http://www.sciencedirect.com/science/article/pii/0022509666900408

Homayonifar, M., Mosler, J., 2011. On the coupling of plastic slip and deformation-induced twinning in magnesium: A variationally consistent approach based on energy minimization. International Journal of Plasticity 27 (7), 983 – 1003.
URL http://www.sciencedirect.com/science/article/pii/S0749641910001786

Homayonifar, M., Mosler, J., 2012. Efficient modeling of microstructure evolution in magnesium by energy minimization. International Journal of Plasticity 28 (1), 1 – 20.
URL http://www.sciencedirect.com/science/article/pii/S0749641911000878

Hong, S.-G., Park, S. H., Lee, C. S., 2010. Role of 10-12 twinning characteristics in the deformation behavior of a polycrystalline magnesium alloy. Acta Materialia 58 (18), 5873 – 5885.
URL http://www.sciencedirect.com/science/article/pii/S135964541000426X

Houtte, P., 1978. Simulation of the rolling and shear texture of brass by the taylor theory adapted for mechanical twinning. Acta Metallurgica 26 (4), 591 – 604.
URL http://www.sciencedirect.com/science/article/pii/0001616078901116

James, R., 1981. Finite deformation by mechanical twinning. Archive for Rational Mechanics and Analysis 77 (2), 143–176.
URL http://dx.doi.org/10.1007/BF00250621

Kadiri, H. E., Baird, J., Kapil, J., Oppedal, A., Cherkaoui, M., Vogel, S. C., 2013. Flow asymmetry and nucleation stresses of twinning and non-basal slip in magnesium. International Journal of Plasticity 44 (0), 111 – 120.
URL http://www.sciencedirect.com/science/article/pii/S0749641912001696

Kalidindi, S., Bronkhorst, C., Anand, L., 1992. Crystallographic texture evolution in bulk deformation processing of {FCC} metals. Journal of the Mechanics and Physics of Solids 40 (3), 537 – 569.
URL http://www.sciencedirect.com/science/article/pii/0022509692800039

Kalidindi, S. R., 2001. Modeling anisotropic strain hardening and deformation textures in low stacking fault energy fcc metals. International Journal of Plasticity 17 (6), 837 – 860.
URL http://www.sciencedirect.com/science/article/pii/S0749641900000711

Kelley, E., Hosford, W. J., 1968a. The deformation characteristics of textured magnesium. TRANS MET SOC AIME 242 (4).

Kelley, E., Hosford, W. J., 1968b. Plane-strain compression of magnesium and magnesium alloy crystals. Trans Met Soc AIME 242 (1), 5–13.

Kochmann, D., Hackl, K., 2011. The evolution of laminates in finite crystal plasticity: a variational approach. Continuum Mechanics and Thermodynamics 23 (1), 63–85.
URL http://www.springerlink.com/content/b02h6085l620u737/?MUD=MP

Kochmann, D., Le, K., 2009. A continuum model for initiation and evolution of deformation twinning. Journal of the Mechanics and Physics of Solids 57 (6), 987–1002.
URL http://www.sciencedirect.com/science/article/pii/S0022509609000325

Kurukuri, S., Worswick, M. J., Ghaffari Tari, D., Mishra, R. K., Carter, J. T., 2014. Rate sensitivity and tension-compression asymmetry in az31b magnesium alloy sheet. Philosophical Transactions of the Royal Society A: Mathematical, Physical and Engineering Sciences 372 (2015).
URL http://rsta.royalsocietypublishing.org/content/372/2015/20130216.abstract

Lee, C., Duggan, B., 1991. A simple theory for the development of inhomogeneous rolling textures. Metallurgical Transactions A 22 (11), 2637–2643.
URL http://dx.doi.org/10.1007/BF02851357

Lee, M., Lim, H., Adams, B., Hirth, J., Wagoner, R., 2010. A dislocation density-based single crystal constitutive equation. International Journal of Plasticity 26 (7), 925 – 938.
URL http://www.sciencedirect.com/science/article/pii/S0749641909001582

Li, B., Ma, E., Jul 2009. Atomic shuffling dominated mechanism for deformation twinning in magnesium. Phys. Rev. Lett. 103, 035503.
URL http://link.aps.org/doi/10.1103/PhysRevLett.103.035503

Lilleodden, E., 2010. Microcompression study of mg (0001) single crystal. Scripta Materialia 62 (8), 532 – 535.
URL http://www.sciencedirect.com/science/article/pii/S1359646209008124

Lou, X., Li, M., Boger, R., Agnew, S., Wagoner, R., 2007. Hardening evolution of {AZ31B} mg sheet. International Journal of Plasticity 23 (1), 44 – 86.
URL http://www.sciencedirect.com/science/article/pii/S0749641906000398

27

Ma, A., Roters, F., 2004. A constitutive model for fcc single crystals based on dislocation densities and its application to uniaxial compression of aluminium single crystals. Acta Materialia 52 (12), 3603 – 3612.
URL http://www.sciencedirect.com/science/article/pii/S1359645404002289

Mielke, A., 2004. Deriving new evolution equations for microstructures via relaxation of variational incremental problems. Computer Methods in Applied Mechanics and Engineering 193 (48-51), 5095 – 5127, advances in Computational Plasticity.
URL http://www.sciencedirect.com/science/article/pii/S0045782504002683

Mosler, J., Ortiz, M., 2006. On the numerical implementation of variational arbitrary lagrangian-eulerian (vale) formulations. International Journal for Numerical Methods in Engineering 67 (9), 1272–1289.
URL http://dx.doi.org/10.1002/nme.1621

Obara, T., Yoshinga, H., Morozumi, S., 1973. $\{11\bar{2}2\}\langle\bar{1}123\rangle$ slip system in magnesium. Acta Metallurgica 21 (7), 845 – 853.
URL http://www.sciencedirect.com/science/article/pii/0001616073901417

Ortiz, M., Repetto, E., 1999. Nonconvex energy minimization and dislocation structures in ductile single crystals. Journal of the Mechanics and Physics of Solids 47 (2), 397 – 462.
URL http://www.sciencedirect.com/science/article/pii/S0022509697000963

Ortiz, M., Repetto, E., Stainier, L., 2000. A theory of subgrain dislocation structures. Journal of the Mechanics and Physics of Solids 48 (10), 2077 – 2114.
URL http://www.sciencedirect.com/science/article/pii/S0022509699001040

Ortiz, M., Stainier, L., 1999. The variational formulation of viscoplastic constitutive updates. Computer Methods in Applied Mechanics and Engineering 171 (3-4), 419 – 444.
URL http://www.sciencedirect.com/science/article/pii/S0045782598002199

Proust, G., Tomé, C. N., Jain, A., Agnew, S. R., 2009. Modeling the effect of twinning and detwinning during strain-path changes of magnesium alloy {AZ31}. International Journal of Plasticity 25 (5), 861 – 880.
URL http://www.sciencedirect.com/science/article/pii/S074964190800079X

Qiao, L., 2009. Variational constitutive updates for strain gradient isotropic plasticity.

Radovitzky, R., Ortiz, M., 1999. Error estimation and adaptive meshing in strongly nonlinear dynamic problems. Computer Methods in Applied Mechanics and Engineering 172 (1-4), 203 – 240.
URL http://www.sciencedirect.com/science/article/pii/S0045782598002308

Reed-Hill, R., Robertson, W., 1958. Pyramidal slip in magnesium. Trans. Met. Soc. AIME 212.

Rice, J., 1971. Inelastic constitutive relations for solids: An internal-variable theory and its application to metal plasticity. Journal of the Mechanics and Physics of Solids 19 (6), 433 – 455.
URL http://www.sciencedirect.com/science/article/pii/002250967190010X

Roberts, E., Partridge, P., 1966. The accommodation around $\{10\bar{1}2\} < 10\bar{1}1 >$ twins in magnesium. Acta Metallurgica 14 (4), 513 – 527.
URL http://www.sciencedirect.com/science/article/pii/0001616066903191

Sandlöbes, S., Zaefferer, S., Schestakow, I., Yi, S., Gonzalez-Martinez, R., 2011. On the role of non-basal deformation mechanisms for the ductility of mg and mg-2013y alloys. Acta Materialia 59 (2), 429 – 439.
URL http://www.sciencedirect.com/science/article/pii/S1359645410005458

Schmidt-Baldassari, M., 2003. Numerical concepts for rate-independent single crystal plasticity. Computer Methods in Applied Mechanics and Engineering 192 (11-12), 1261 – 1280.
URL http://www.sciencedirect.com/science/article/pii/S0045782502005637

Schröder, J., Neff, P., Ebbing, V., 2008. Anisotropic polyconvex energies on the basis of crystallographic motivated structural tensors. Journal of the Mechanics and Physics of Solids 56 (12), 3486 – 3506.
URL http://www.sciencedirect.com/science/article/pii/S0022509608001373

Simo, J., 1988a. A framework for finite strain elastoplasticity based on maximum plastic dissipation and the multiplicative decomposition: Part i. continuum formulation. Computer Methods in Applied Mechanics and Engineering 66 (2), 199 – 219.
URL http://www.sciencedirect.com/science/article/pii/004578258890076X

Simo, J., 1988b. A framework for finite strain elastoplasticity based on maximum plastic dissipation and the multiplicative decomposition. part ii: Computational aspects. Computer Methods in Applied Mechanics and Engineering 68 (1), 1 – 31.
URL http://www.sciencedirect.com/science/article/pii/0045782588901041

Slutsky, L. J., Garland, C. W., Aug 1957. Elastic constants of magnesium from 4.2 k to 300 k. Phys. Rev. 107, 972–976.
URL http://link.aps.org/doi/10.1103/PhysRev.107.972

Stanford, N., Sotoudeh, K., Bate, P., 2011. Deformation mechanisms and plastic anisotropy in magnesium alloy {AZ31}. Acta Materialia 59 (12), 4866 – 4874.
URL http://www.sciencedirect.com/science/article/pii/S1359645411002709

Staroselsky, A., Anand, L., 2003. A constitutive model for hcp materials deforming by slip and twinning: application to magnesium alloy {AZ31B}. International Journal of Plasticity 19 (10), 1843 – 1864.
URL http://www.sciencedirect.com/science/article/pii/S0749641903000391

Taylor, G., 1938. Plastic strain in metals. J. Inst. Met. 62, 307–324.

Tegart, W. J. M., 1964. Independent slip systems and ductility of hexagonal polycrystals. Philosophical Magazine 9 (98), 339–341.
URL http://dx.doi.org/10.1080/14786436408229197

Thoutireddy, P., Ortiz, M., 2004. A variational r-adaption and shape-optimization method for finite-deformation elasticity. International Journal for Numerical Methods in Engineering 61 (1), 1–21.
URL http://dx.doi.org/10.1002/nme.1052

Ulacia, I., Dudamell, N., Glvez, F., Yi, S., Prez-Prado, M., Hurtado, I., 2010. Mechanical behavior and microstructural evolution of a mg {AZ31} sheet at dynamic strain rates. Acta Materialia 58 (8), 2988 – 2998.
URL http://www.sciencedirect.com/science/article/pii/S1359645410000431

28

von Mises, R., 1928. Mechanik der plastischen Formaenderung von Kristallen. Zeitschrift f. Angewandte Mechanik 8, 161–185.
   URL http://www.wiley-vch.de/vch/journals/2231/pss40/241_250.pdf

Wang, H., Wu, P., Tomé, C., Huang, Y., 2010. A finite strain elastic viscoplastic self-consistent model for polycrystalline materials. Journal of the Mechanics and Physics of Solids 58 (4), 594 – 612.
   URL http://www.sciencedirect.com/science/article/pii/S0022509610000050

Wonsiewicz, B., Backofen, W., 1967. Independent slip systems and ductility of hexagonal polycrystals. Transaction of Metallurgical Society of AIME 239, 1422–1433.

Yang, Q., Stainier, L., Ortiz, M., 2006. A variational formulation of the coupled thermo-mechanical boundary-value problem for general dissipative solids. Journal of the Mechanics and Physics of Solids 54 (2), 401 – 424.
   URL http://www.sciencedirect.com/science/article/pii/S0022509605001511

Yoshida, K., Brenner, R., Bacroix, B., Bouvier, S., 2009. Effect of regularization of schmid law on self-consistent estimates for rate-independent plasticity of polycrystals. European Journal of Mechanics - A/Solids 28 (5), 905 – 915.
   URL http://www.sciencedirect.com/science/article/pii/S0997753809000618

Yu, Q., Qi, L., Chen, K., Mishra, R. K., Li, J., Minor, A. M., 2012. The nanostructured origin of deformation twinning. Nano Letters 12 (2), 887–892, pMID: 22239446.
   URL http://dx.doi.org/10.1021/nl203937t

Zhang, J., Joshi, S. P., 2012. Phenomenological crystal plasticity modeling and detailed micromechanical investigations of pure magnesium. Journal of the Mechanics and Physics of Solids 60 (5), 945 – 972.
   URL http://www.sciencedirect.com/science/article/pii/S0022509612000130

29